

Coastal topography and hydrogeology control critical groundwater gradients and potential beach surface instability during storm surges~~Hydrogeological controls on the spatio-temporal variability of surge-induced hydraulic gradients along coastlines: implications for beach surface stability~~

Anner Paldor¹, Nina Stark², Matthew Florence², Britt Raubenheimer³, Steve Elgar³, Rachel Housego^{3,4}, Ryan S. Frederiks¹, Holly A. Michael^{1,5}

¹ Department of Earth Sciences, University of Delaware, Newark, DE, USA.

² Department of Civil and Environmental Engineering, Virginia Polytechnic Institute and State University, Blacksburg, VA, USA.

³ Department of Applied Ocean Physics and Engineering, Woods Hole Oceanographic Institution, Woods Hole, MA, USA.

⁴ MIT-WHOI Joint Program in Oceanography, 86 Water St., Woods Hole, MA, USA.

⁵ Department of Civil and Environmental Engineering, University of Delaware, Newark, DE, USA.

Correspondence to: Holly A. Michael (hmichael@udel.edu)

Abstract. Ocean surges pose a global threat for coastal stability. These hazardous events alter flow conditions and pore pressures in flooded beach areas during both inundation and subsequent retreat stages, which can mobilize beach material, potentially enhancing erosion significantly. In this study, the evolution of surge-induced pore-pressure gradients is studied through numerical hydrologic simulations of storm surges. The spatiotemporal variability of critically high gradients is analyzed in 3D. The analysis is based on a threshold value obtained for ~~momentary liquefaction~~quicksand formation of beach materials under groundwater seepage. Simulations of surge events show that during the run-up stage, head gradients can rise to the calculated critical level landward of the advancing inundation line. During the receding stage, critical gradients were simulated seaward of the retreating inundation line. These gradients reach maximum magnitudes just as sea level returns to pre-surge level, and are most accentuated beneath the still-water shoreline, where the model surface changes slope. The gradients vary along the shore owing to variable beach morphology, with the largest gradients seaward of intermediate-scale (1-3m elevation) topographic elements (dunes) in the flood zone. These findings suggest that the common practices in monitoring and mitigating surge-induced failures and erosion, which typically focus on the flattest areas of beaches, might need to be revised to include other topographic features.

28 1 Introduction

29 Groundwater seepage can destabilize land areas, especially at the interface between terrestrial and submerged systems
30 (Iverson, 1995; Iverson & Major, 1986; Iverson & Reid, 1992; Schorghofer et al., 2004; Stegmann et al., 2011). Recent studies
31 have examined the characteristics of pore pressure behavior, the associated groundwater seepage, and its effect on the stability
32 of geomaterials (soils, rocks, etc.), including field observations (Mory et al., 2007; Sous et al., 2016), physical experiments
33 (Schorghofer et al., 2004; Sous et al., 2013), numerical simulations (Orange et al., 1994; Rozhko et al., 2007; Schorghofer et
34 al., 2004), and analytical models (Sakai et al., 1992; Yeh & Mason, 2014). There are several examples of seepage-induced
35 failure of the surface (i.e. the mobilization of the soil skeleton) from around the world, including Japan (Yeh & Mason, 2014),
36 California (Orange et al., 2002), and France (~~Sous et al., 2016~~; Stegmann et al., 2011).

37 Soil liquefaction and quicksand occurs when pore pressures in the geomaterial rise to a point where its effective stress drops
38 to zero and the material is fluidized, and thus acts as a liquid. The distinction between the two terms related to the mechanism
39 inducing the rise in pore pressures, with liquefaction referring to cases where external forces (e.g., earthquakes) are involved.
40 Quicksand is used for cases where the pore pressures rise due to intrinsic changes in the groundwater regime. At the coast,
41 ocean (waves, surge, tides, inundation) and terrestrial (groundwater heads, precipitation, and overland flows) processes
42 concurrently contribute to changing pore pressures in beach and nearshore sediments, and ~~changes in pore pressure~~
43 ~~distributions and gradients~~ could thus induce failure of the surface. Ocean effects on pore pressures, groundwater flow, and
44 seepage occur due to wind waves, storm surges, and tsunamis. For example, a 1D analytical model suggests that during a
45 tsunami, vertical hydraulic gradients can destabilize sediments and increase the potential for sediment momentary liquefaction,
46 consistent with laboratory experiments (Abdollahi & Mason, 2020; Yeh & Mason, 2014). Laboratory experiments (Sous et al.,
47 2013) suggest that the magnitudes of hydraulic gradients in the beach due to infiltration from sea-swell and infragravity waves
48 depend on the wave frequency, cross-shore position, water table overheight, and the presence of standing waves. A large-scale
49 (250 m) flume study of a barrier island showed that waves can alter the coastal groundwater head distribution significantly,
50 and can change cross-island and local (under the ocean beach) hydraulic gradient directions (Turner et al., 2016). Field
51 observations of pore pressures over several tidal cycles in a microtidal beach (Sous et al., 2016) suggest that breaking-wave-
52 driven onshore increases in the water surface (setup) over the 10 m nearest the shoreline induced groundwater head changes
53 of O(0.1 m) (Sous et al., 2016). Furthermore, density-driven flow at the subsurface transition zone between fresh terrestrial
54 groundwater and saline groundwater can produce intense, localized seepage (Burnett et al., 2006). Rapid changes in seepage
55 characteristics (locations, magnitudes, direction) during extreme events may lead to sediment liquefaction-quicksand (i.e., loss
56 of particle-to-particle contacts and sediment effective stresses) and sediment mobilization, resulting in erosion and structure
57 destabilization.

58 *Observations, theories, and simulations have shown that the pore-pressure changes owing to energetic ocean waves can*
59 *reduce effective stresses and may cause liquefaction failure of structures and surfaces (Chini & Stansby, 2012; Mory et al.,*
60 *2007; Sakai et al., 1992; Sous et al., 2013; Yeh & Mason, 2014 Michallet et al., 2009). Measured pore-pressure changes in*

beach sediments during intense waves suggest that momentary liquefaction and quicksand may occur at shallow depths (<1 m) below the surface (Mory et al., 2007), consistent with theory (Sakai et al., 1992). Analytical solutions for the effective stress in an idealized seabed suggest that waves can alter the stresses in the upper meters of the seafloor significantly (Mei & Foda, 1981; Sakai et al., 1992). Simulations of a theoretical 2D porous medium, where an increase in pore pressure is applied at the bottom of the layer from a point source, revealed that different spatial failure patterns (i.e. the geometry of the slip surface) can occur under various stress regimes (i.e. distribution of stresses in the soil) (Rozhko et al., 2007), although the process that leads to the simulated change in the pore-pressure distribution was unexplored.

Apart from waves, storm surges also could alter the onshore hydrogeological regime and potentially reduce the stability of the beach surface, ~~yet surges have not been explored in this context~~. Recently, (S. Yang & Tsai, 2020) modelled groundwater response to coastal flooding in the New Orleans greater area, and found that the interaction between flood water and surface water may destabilize levees in the area. This work focuses on the influence of alongshore topography and hydrogeological factors on geotechnical impacts near the shoreline owing to ocean surges driven by coastal storms, which are projected to intensify and become more frequent in the future (Chini & Stansby, 2012; Tebaldi et al., 2012). In particular, the three-dimensional dynamics of surge-induced ~~inundation-flooding~~ and the resulting shore-parallel distribution of pore-pressure gradients in sandy beach areas are not well understood. Specific questions addressed in this work are: (1) Can surge-induced pore pressure changes promote sediment ~~liquefaction-quicksand~~ of the uppermost sediment layers (<5 m), and which areas across the beach are the most vulnerable? (2) What is the relationship between beach morphology and the spatio-temporal evolution of pore pressure gradients? (3) How do the hydrogeological properties (hydraulic conductivity, groundwater recharge) of the coastal system affect the potential for failure? Field evidence is presented for the effect of storm surges on coastal groundwater heads (Section 2), a criterion is derived (Section 3) for ~~momentary soil liquefactionquicksand~~ for beach slopes with groundwater discharge based on existing solutions (Briaud, 2013), and a model framework is described (Section 4) and used to simulate surges in theoretical beach settings and to examine their effect on sediment stability (Section 5).

83 ~~2 Field evidence for hydraulic head changes during storm surges~~

~~Groundwater observations collected every 10 min from October 2014 to November 2017 in 8 wells deployed across a 500-m wide barrier island on the Outer Banks of NC, near the town of Duck (Figure 1a) indicate that coastal storm waves and surge significantly affect the freshwater equivalent heads from the beach to more than 310 m inland of the beach (Housego et al., 2018). The study period included 27 storm events (including 4 hurricanes) in which wave heights measured in 26-m water depth (NDBC Station 44100) often exceeded 3.5 m, surge (NOAA tide gauge 8651371) was between 0.5 and 1.0 m, and 36-hr averaged (to remove fluctuations owing to tides and wind wave motions) shoreline water levels increased from about 0.6 to 2.4 m owing to surge and wave-driven setup (included in the simulated surge height). In response to the increased ocean water levels, the groundwater level under the ocean dunes rose 0.5 to 2.0 m. For example, following the passage of Hurricane Joaquin in 2015, which caused offshore wave heights of 4.7 m (and <1 cm of rainfall), head levels under the ocean dunes and 25, 90, 160, and 310 m farther inland increased 1.6, 1.4, 1.2, 0.9, and 0.5 m above pre-storm levels, respectively (Figure 1b). These and other storm-driven increases in head levels changed the direction of the hydraulic gradient from toward the bay (inland) during calm conditions to toward the~~

ocean during storms (compare black and red points in Figure 1b under calm conditions with those during the storm). After the shoreline water level returns to pre-storm conditions, the water table behind the dune remains elevated and groundwater discharges back out through the beach as the water table recovers. During the storm, the horizontal location of the shoreline remained more than 10 m seaward of the dunes, and thus there was no inundation from overtopping, which could increase groundwater levels even farther inland. Changes in hydraulic gradients, including the effects of inundation, are investigated in Section 4 with a numerical model that does not mimic the conditions in this field site, but is a generalized representation of coastal hydrogeological systems.

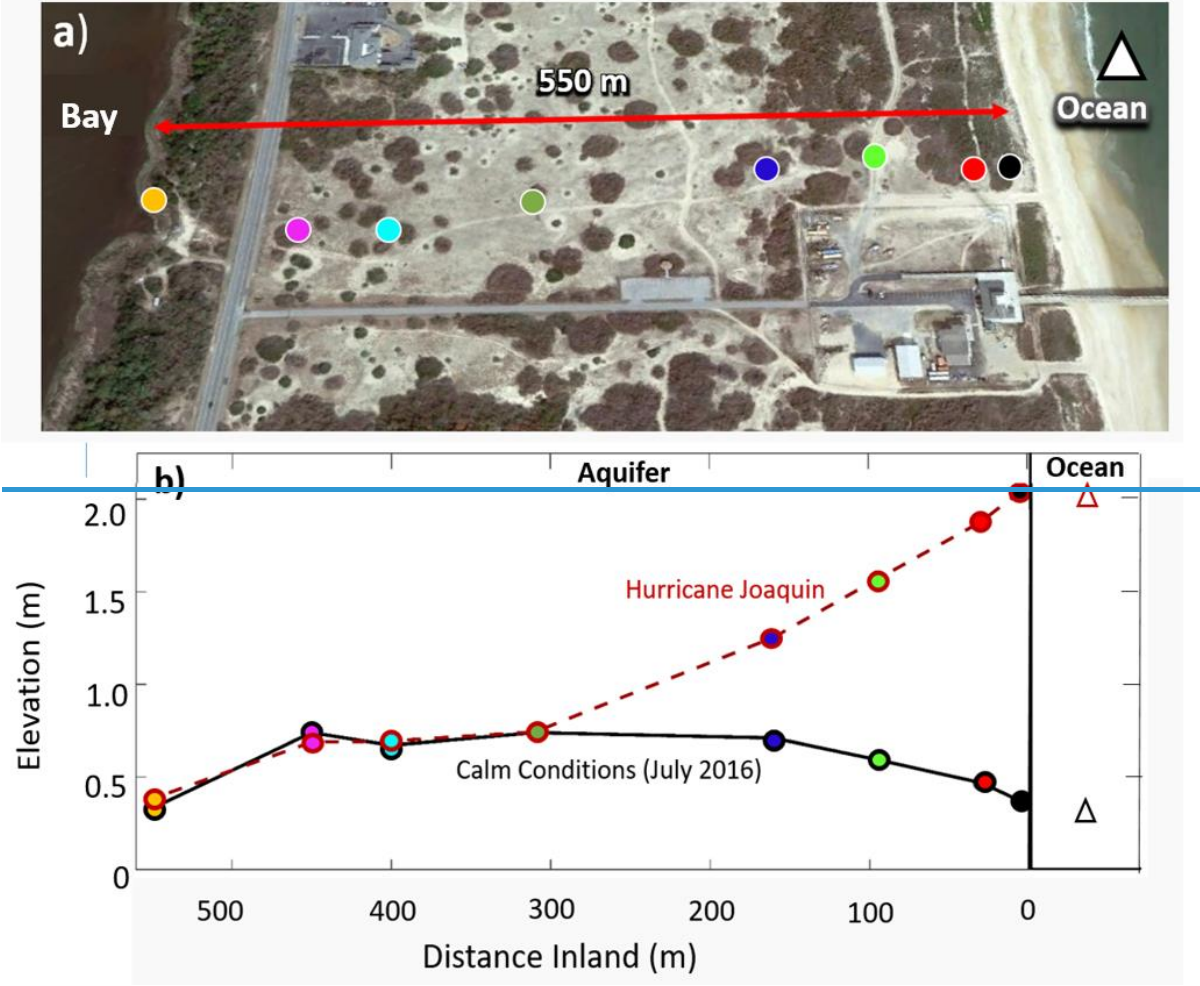


Figure 1: a) Google Earth image of the Outer Banks near Duck, NC, with the locations of groundwater wells (colored circles). (b) Elevation of the ocean level (triangles) and 36-hr avg. freshwater equivalent groundwater heads (circles) vs. inland distance from the dune ($x=0$ m). Colors correspond to colors of symbols in (a) for the average of the calm conditions in July 2016 (black triangle and circle outlines connected by black lines) and at the peak of Hurricane Joaquin (red triangle and circle outlines connected by red dashed lines).

110 **3.2 Conceptual model and governing equations**

111 A conceptual model of a coastal system (Figure 2.1) includes infiltration of rain that recharges the aquifer with freshwater,
112 resulting in fresh groundwater flow toward the ocean. In the nearshore area (typically within meters of the shoreline), an
113 inclined freshwater-saltwater transition zone develops between the saline groundwater underlying the seafloor and the
114 terrestrial fresh groundwater. The density gradient at the transition zone deflects the fresh groundwater flow upward, and
115 produces focused groundwater discharge near the coastline that can be amplified by an order of magnitude or more relative to
116 the average flow rate in the aquifer (Paldor et al., 2020). In phreatic aquifers, submarine groundwater discharge typically occurs
117 within tens of meters of the coastline, depending on the recharge rates and aquifer properties (Bratton, 2010). In systems where
118 the discharge is into a body of freshwater (e.g., a lake), the bottom of the lake is a constant head boundary, and thus the seepage
119 is, by definition, perpendicular to the lakebed. This assumption is widely adopted in geotechnical calculations of groundwater
120 discharge magnitudes. For example, in flow net solutions for classic dam and levee problems, the bottom of the river on both
121 sides of the dam or levee is considered an equipotential line (Briaud, 2013). However, along the bottom of a saltwater body
122 the freshwater-equivalent head is variable with bathymetry, and hence the seepage is not necessarily perpendicular to the
123 seafloor and possibly represents a complex, three-dimensional problem with high spatiotemporal variability. To assess the risk
124 of ~~liquefaction-quicksand~~ in the context of the freshwater-saltwater transition zone and during coastal ~~inundation-flooding~~
125 events, the vertical component of the hydraulic gradient is computed to evaluate the potential for ~~liquefaction-quicksand~~ (as
126 will be derived in the following section) with the application of the variable-head boundary condition and the inclusion of
127 variable-density flow solutions. It should be highlighted that in the current work, no effects of long-term loading and residual
128 liquefaction were investigated. Hereinafter, the vertical hydraulic gradients will be discussed rather than the pore pressures or
129 heads. In the next section the equations for soil failure potential in terms of the head gradients are derived based on previous
130 derivations (Briaud, 2013). The magnitude of the hydraulic head gradient (~~Figure 2~~), which according to Darcy's law is the
131 magnitude of the seepage vector divided by the hydraulic conductivity, is denoted i (Figure 1). The seepage vector is the
132 specific discharge, which is computed as the outflow vector at top nodes of the domain. In 2D, this vector has two components
133 – a horizontal ($-Ki_x$ in Figure 1) and a vertical ($-Ki_z$). This work focuses on the vertical component. Other variables used in the
134 following calculations are shown in Figure 2.1 and summarized in Table 1.

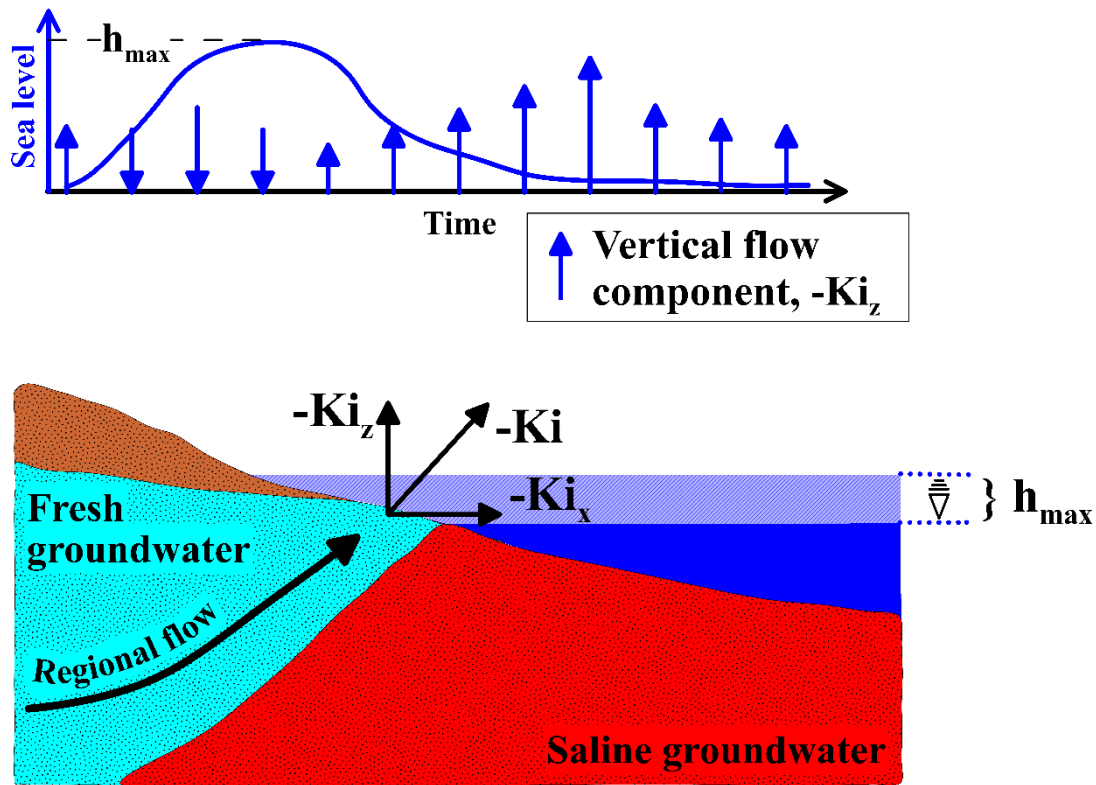


Figure 21: A typical-hypothetical coastal hydrogeological system. Regional fresh (light blue) groundwater flows to the sea and upward due to variable-density flow along the freshwater-saltwater (red) interface. In the nearshore area, focused groundwater discharge occurs either into the sea (blue) or along a seepage face onshore. As shown in the top of the figure, when the surge begins, the direction of flow reverses (infiltration), and when the sea level reaches its maximal level (h_{\max}) the surge retreats and the direction reverts back (exfiltration). The upward (positive vertical component) of flow reaches a maximum when the sea level is back to pre-surge level, before decaying to the steady-state magnitude.

152 Table 1: Variables used in the theoretical calculations and numerical simulations.

Parameter	Symbol	Value	Unit	Source
Hydraulic conductivity	K	10-100	m/d	Freeze & Cherry (1979)
Anisotropy	K_x/K_z	10		
Seawater density	ρ_{sw}	1025	Kg/m ³	
Freshwater density	ρ_{fw}	1000	Kg/m ³	
Local water density	ρ_w	1000- 1025	Kg/m ³	
Solid material density	ρ_s	2650	Kg/m ³	
Unit weight of water	γ_w	10⁴	N/m³	Briaud (2013)
Unit weight of saturated soil	γ_{sat}		N/m³	
Freshwater influx	q_0	0.01-0.04	m/d	
Aquifer storativity	S_s	10 ⁻⁴	1/m	Freeze & Cherry (1979)
Porosity	n	0.3		
Longitudinal/Transverse Dispersivity	α_L/α_T	1/0.1	m	Gelhar et al. (1992)
Maximum surge height	h_{0max}	3	m	Chini & Stansby (2012)

153

154 **32.1 The criterion for [liquefaction-quicksand](#) under groundwater seepage**

155 ~~Some publications distinguish between the Two~~ terms ~~that are often confused are~~ “liquefaction” and “~~quick sand~~[quicksand](#)”,
156 with the former being used for earthquake-induced fluidization of the soil, and the latter being related to failure due to upward
157 flow (Briaud, 2013). ~~However, the The~~ physical meaning of the two is ~~the same similar~~ – geomaterial becoming
158 ~~weightless~~[suspended in a colloidal solution](#), which can result in erosion and sediment mobilization, or loss of support of any
159 infrastructure built into the soil. Here, the term [liquefaction-quicksand](#) is used, ~~although as~~ the analysis refers to surge-induced
160 changes in the subsurface flow rather than seismically induced flows. Following Briaud (2013), [quicksand](#) ~~liquefaction~~ occurs
161 when the pore pressure (u_w) at a certain depth (z) exceeds the total stress (σ), i.e. when the effective stress (σ') goes to zero:

162

$$\sigma' = \sigma - u_w \leq 0 \tag{1}$$

163 Neglecting the possibility that gas is still trapped in the pores and assuming a submerged unit weight can be applied, the
 164 criterion for localized, ~~momentary liquefaction~~ quicksand in inundated regions can be written in a gradient form (Goren et al.,
 165 2013), in which the vertical pore pressure gradient (positive downward gradient generates upwards flow) exceeds the
 166 submerged unit weight of the soil (γ_{sub}):

$$\gamma_{sub} + \frac{\partial u_w}{\partial z} \leq 0 \quad (2)$$

167 where

$$\gamma_{sub} = (1 - n) \cdot (\rho_s - \rho_{fw}) \cdot g \quad (3)$$

168
 169 in which ρ_s is the density of the beach material (sand), and ρ_w is the density of the local water, which has a value between that
 170 of seawater ($\rho_{sw} \approx 1025 \text{ kg/m}^3$) and freshwater ($\rho_{fw} \approx 1000 \text{ kg/m}^3$). This failure criterion is similar to Yeh and Mason
 171 (2014), who studied liquefaction of a fully saturated sediment following a tsunami.

172 The constant value of porosity ($n=0.3$) is typical for sandy soils, but neglects localized variations in sand bulk density in the
 173 simulated areatopography. ~~Furthermore, it is noted that the use of the submerged unit weight of soil is likely an~~
 174 ~~underestimate of the actual unit weight for soils under storm surge conditions, since saturated conditions may prevail prior to~~
 175 ~~inundation and the saturated unit weight is higher than the submerged ($\gamma_{sub} = \gamma_{sat} - \gamma_{fw}$). The use of γ_{sub} as the~~
 176 ~~representative unit weight of simulated soil is appropriate for soils that are fully submerged, as it accounts for the buoyancy~~
 177 ~~effect, considering the unit weight of the overlying water column (γ_w). However, for the parts of the model landward of the~~
 178 ~~inundation line, the saturated unit weight may be more suitable. This means that adopting γ_{sub} uniformly may be an~~
 179 ~~underestimate of the actual unit weight in real systems ($\gamma_{sub} = \gamma_{sat} - \gamma_w$). However~~ Nevertheless, we used γ_{sub} since the aim
 180 of this work ~~aims is~~ to harness a hydrologic modelling framework to assess the spatio-temporal distribution of surge-induced
 181 changes in hydraulic gradients. To that end, the liquefaction-quicksand assessment is limited to the effects of vertical
 182 pressure gradients, ~~momentary liquefaction~~, and the application of the submerged unit weight. It should be noted that studies
 183 have shown partially saturated sediments (e.g., in inundation areas) are typically prone to momentary liquefaction (Mory et
 184 al., 2007; Yeh and Mason, 2014). Mory et al. (2007) showed that even a 6% air content may alter-increase the potential for
 185 momentary liquefaction. For the gradient-form criterion to hold, this condition would need to be met continuously from the
 186 surface to the depth of the liquefied layer (Goren et al. 2013), as accounted for in the analysis below.

187 Here, the ~~momentary liquefaction-quicksand~~ criterion is related to vertical components of seepage vectors to compare the
 188 results of the groundwater model with the failure criterion. The 3D model considered here (see below) could be used to examine
 189 the horizontal components too, and to analyze the potential for shear failure, not only for quicksand and momentary
 190 liquefaction (Zen et al., 1998). However, for the sake of simplicity and in the interest of focusing on the questions addressed
 191 here, such an expansion is not attempted in the current study. It would require further assumptions on the soil characteristics
 192 (internal friction, cohesion) and a localized analysis of the local slopes for each point in the domain. According to Darcy's law

193 the vertical ~~flow velocities~~specific discharge (denoted v_z with dimensions $[MT^{-1}]$) ~~are~~is equal to the product of the (local)
 194 vertical head gradient and the vertical hydraulic conductivity K_z :

$$v_z = -K_z \left(\frac{1}{\rho_{fw}g} \frac{\partial u_w}{\partial z} + 1 \right) \quad (4)$$

195
 196 thus, the vertical pressure gradient becomes

$$\frac{\partial u_w}{\partial z} = -\rho_{fw}g \left(\frac{v_z}{K_z} + 1 \right) \quad (5)$$

197
 198 Substituting Equations 3 and 5 into Equation 2 yields:

$$(1 - n) \cdot (\rho_s - \rho_{fw}) \cdot g - \rho_{fw}g \left(\frac{v_z}{K_z} + 1 \right) \leq 0 \quad (6)$$

199
 200 From Equation 6, the value of the critical vertical head gradient (i_c) is that above which the effective stress is zero or less:

$$\left(\frac{v_z}{K_z} \right)_c \equiv i_c = (1 - n) \cdot \frac{\rho_s - \rho_{fw}}{\rho_{fw}} - 1 \quad (7)$$

201 This result is similar to that derived by Briaud (2013) ~~for a general case of quicksand, but h~~Here it is derived specifically to
 202 facilitate for saturated groundwater flow, which is the appropriate formulation for the scenario of direct calculations of surge-
 203 induced changes in the groundwater flow regime as output by the hydrologic model. Using Darcy's law in this context assumes
 204 that during the surge the groundwater flow remains largely laminar, which is likely for storm-surge conditions and is a common
 205 assumption in similar studies (Abdollahi & Mason, 2020; Guimond & Michael, 2021; Paldor & Michael, 2021; J. Yang et al.,
 206 2013; Yu et al., 2016). For convenience, the magnitude of downward (negative-(destabilizing)) vertical head gradients which
 207 initiate upward (positive) vertical velocities and therefore potentially destabilize the soil, is hereinafter denoted i_z and
 208 presented in positive values. Using typical values for porosity, solid particle density, and freshwater density for beach material
 209 ($n = 0.3$; $\rho_s = 2650 \text{ kg/m}^3$; $\rho_{fw} = 1000 \text{ kg/m}^3$, respectively), Equation 7 suggests the critical value of vertical head
 210 gradient is about $i_c = 0.15$. While the parameters can have ranges of values for given systems, Thethe following analyses use
 211 this value as a threshold for liquefactionquicksand, with simulated values of i_z normalized by the critical value $i_c = 0.15$ as
 212 the seepage-liquefaction factor (SLF):

$$SLF = \frac{i_z}{i_c} \quad (8)$$

213 We term the criterion seepage-liquefaction factor, while it is noted again that the actual failure mechanism discussed here is
 214 quicksand as it is not related to seismic loading. In Equation 8, i_z is the actual simulated or observed vertical head gradient,
 215 defined as $i_z = -\frac{v_z}{K_z}$ (Eq. 4) and i_c is the theoretical liquefaction-quicksand threshold (Eq. 7). Thus, any point in space and

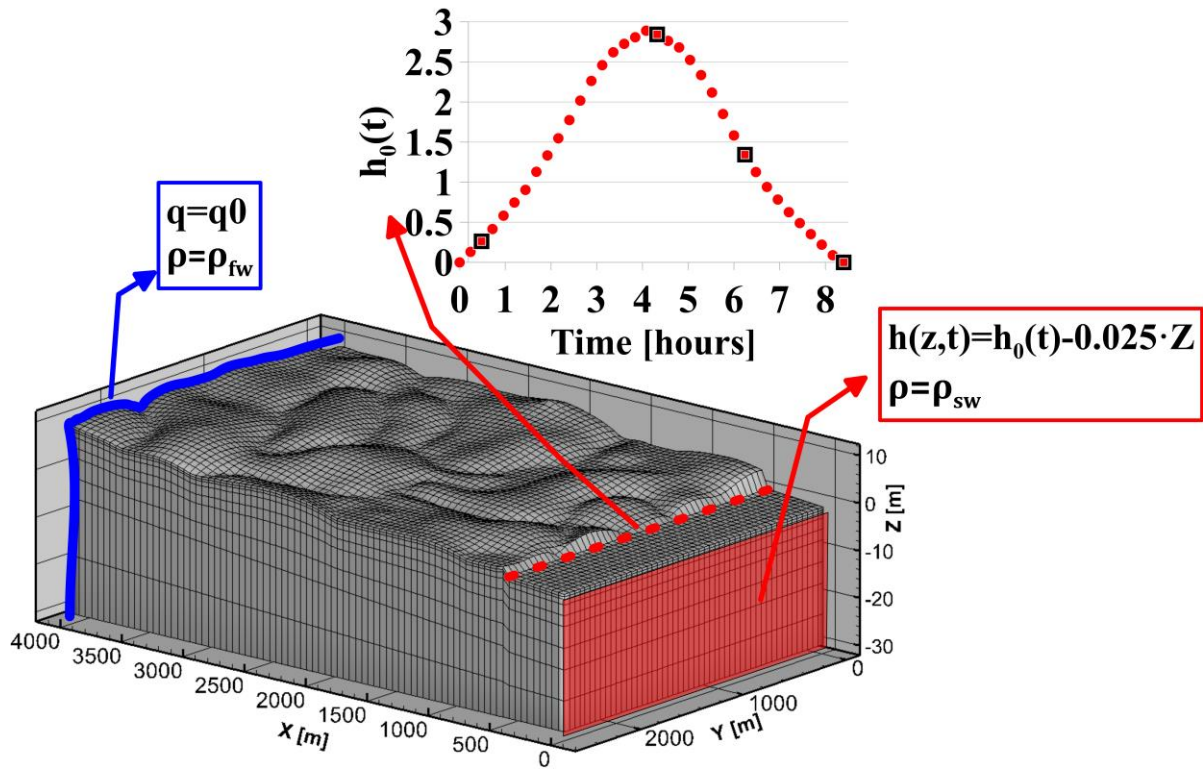
time in which simulated SLF is close to 1 is potentially nearing ~~liquefaction~~quicksand. A layer in which SLF approaches 1 continuously from the surface to a depth Z_l is considered a “critical layer” of thickness Z_l . The SLF defined here is the reciprocal of the Factor of Safety defined by Yang and Tsai (2020) for levees under storm-induced groundwater seepage, and thus it should be noted that in the analysis presented here lower values of SLF represent greater stability.

4.3 Hydrologic model

The effect of storm surges on groundwater flow is simulated using Hydrogeosphere (HGS) – a 3D numerical code that couples surface and subsurface flow and solute transport (Therrien et al., 2010). For the surface flow, HGS solves the Saint-Venant equations (also known as nonlinear shallow water equations), and for the variably saturated subsurface flow it solves the Richards equation. The salt transport equation is solved in its advective-dispersive form, and the variable-density flow solution is coupled to the transport solution through a linear equation of state. Hydrogeosphere has been successfully employed to simulate storm surges in several recent studies (Guimond & Michael, 2020; Yang et al., 2013, 2018; Yu et al., 2016), and here it is applied to assess the risk for ~~sediment liquefaction~~quicksand and erosion from surge-induced pore water head gradients. ~~This is a novel interdisciplinary approach, applying a robust 3D hydrologic model in the context of coastal geomechanics. This interdisciplinary approach, using a groundwater model in the context of coastal geomechanics, has recently been applied by Yang and Tsai (2020) to assess the impacts of floods on the groundwater regime in the Greater New Orleans area, and its implications for the factor of safety of levees. Several other studies have also applied different methods to relate between changes in the groundwater regime and the stability of the surface (Chini & Stansby, 2012; Sakai et al., 1992; Sous et al., 2013; Yeh & Mason, 2014). The novelty in this study relates to the harnessing of a 3D integrated hydrologic model in a generalized form to explore the mechanisms that dominate surge-induced quicksand formation. Applying the fully-coupled model on different generalized topographies (detailed below) allows us to study the alongshore distribution of critical gradients, which is commonly overlooked in similar studies (Yeh and Mason, 2014).~~

The model domain (Figure 32) is 4000 m (cross-shore, X) by 2500 m (alongshore, Y), extending to a depth of 30 m below the mean sea level ($Z=0$). The terrestrial extent of the domain is 3550 m ($450 < X \leq 4000$), with the ocean spanning $0 \leq X \leq 450$ (Figure 32). The elevation at the ocean side boundary is $Z(X=0)=-1$, so the seafloor slope is $1/450 \approx 0.0022$. This slope is representative of U.S. Atlantic and Gulf coastal systems averaged over large cross-shore distances (e.g., from the beach to the mid continental shelf). Although local slopes in the surf and beach often are much steeper than those used here, this study is focused on the ~~liquefaction-quicksand potential~~ in and near the inundated dune system. The average surface elevation inland ($X=4000$ m) is 5 m, so that the average land surface slope is $5/3550 \approx 0.0014$. Thus, there is a change in average slope at the coastline, as the offshore portion is steeper (~ 0.0022) than the onshore (0.0014), as in many coastal areas. ~~To justify this setting, A-we ran a simulation with a -0.5 m sea level (i.e., still water shoreline at $X=225$ m), which indicates-indicated that critical vertical hydraulic gradients occur near this change in overall slope irrespective of the shoreline location (Figure A1 in the Appendices). A simulation with a larger beach slope ($Z(X=0)=-6$; slope= $6/450=0.0130$) resulted in similar vertical hydraulic gradients as~~

248 the baseline slope (0.0022) (Figure A2 in the Appendices), indicating that although the baseline slope is lower than typical,
 249 the analysis based on it is also valid for steeper slopes. The domain of the finite difference model consists of 44,000 rectangular
 250 cells, where the cell sizes in the X and Y direction are 25 and 50 m, respectively. The cell size in the Z direction varies from 8
 251 m in the bottom of the domain to about 0.5 m in the top 2 m to balance between computation time and the resolution necessary
 252 to resolve the dynamics close to the surface (Figure 32). The homogenous hydraulic conductivity K_x is 50 m/d for the baseline
 253 simulation, and values of $K_x = 10, 25, 100$ m/d were also simulated as part of a sensitivity analysis and K_x varied between 10
 254 and 100 m/d in sensitivity analyses. In all simulations, the anisotropy was 10 (i.e., the vertical hydraulic conductivity, K_z , was
 255 10 times lower than the horizontal hydraulic conductivity, K_x). This range of hydraulic conductivity with a porosity, n , of 0.3
 256 is typical for sandy beach environments (Freeze and Cherry, 1979). Anisotropy of porous material may represent the presence
 257 of horizontally-extended low-K lenses (e.g., localized compacted clay lenses), which reduce the conductivity in the vertical
 258 dimension preferentially. Although a change in K could be associated with a change in n for some sediments and mixtures,
 259 due to the potentially complex relationships between porosity and the sediment textural properties, including grain size
 260 distributions, shapes, and K , the porosity was kept constant in the simulations presented here.



261
 262 **Figure 32:** Hydrogeosphere model domain as a function of the vertical Z, cross-shore X, and alongshore Y dimensions, boundary
 263 conditions (red and blue boxes), and the surge height evolution curve (inset). The blue curve is the terrestrial freshwater recharge
 264 boundary, the red rectangle is where a fixed seawater head and concentration are applied to the subsurface domain, and the red
 265 dashed line is where the sea level height boundary condition ($h_0(t)$) is applied on the surface domain. For the steady-state

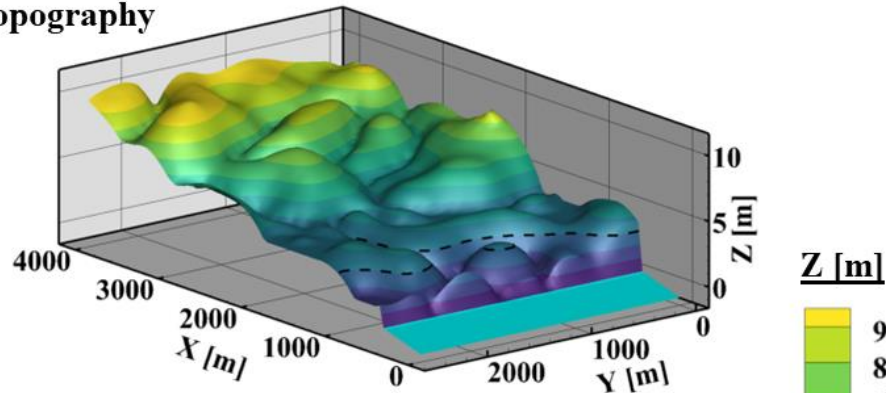
simulations $h_0(t)=0$, and for the transient simulations the curve in the inset is applied. The black squares in the inset mark the times plotted in Figure 54.

The boundary conditions in the simulations were applied in two stages – a steady-state period and a transient surge period. For the steady-state simulations, terrestrial boundary conditions of constant freshwater specific recharge ($q=q_0, \rho=\rho_{fw}$) were applied on the vertical wall at the inland edge of the subsurface domain at $X=4000$ (blue curve in Figure 32) (Ataie-Ashtiani et al., 2013; Yang et al., 2018; Yu et al., 2016). The opposite edge of the domain at $X=0$ (red wall in Figure 32) was a typical sea boundary condition with depth-dependent head and saline ocean water ($h=-0.025 \cdot Z$; $\rho=\rho_{sw}$). On the surface domain the only boundary condition is applied on the coastline $X=450$ m, red dashed line in Figure 32 as a fixed, time-dependent head ($h=h_0(t)$) and seawater density ($\rho=\rho_{sw}$). The applied head on the coastline was held at zero through the steady-state simulations. For the transient surge simulations, the coastline head was varied over 8.5 hours between zero and a 3 m maximum surge height (inset in Figure 32). A sea level of 3 m above the mean represents a combined high-tide and surge event with a projected return period of 100 yr by the year 2050 in the East Coast of the United States (Tebaldi et al., 2012). The ocean surface was assumed to be spatially constant at any time, and effects of wind waves were not simulated. The simulated surge height is comparable in magnitude to macro-tides, but the differences in frequency (macro-tides are diurnal) mean that macro-tidal beaches are likely in equilibrium with respect to sediment mobility, which is not the case for storm surges.

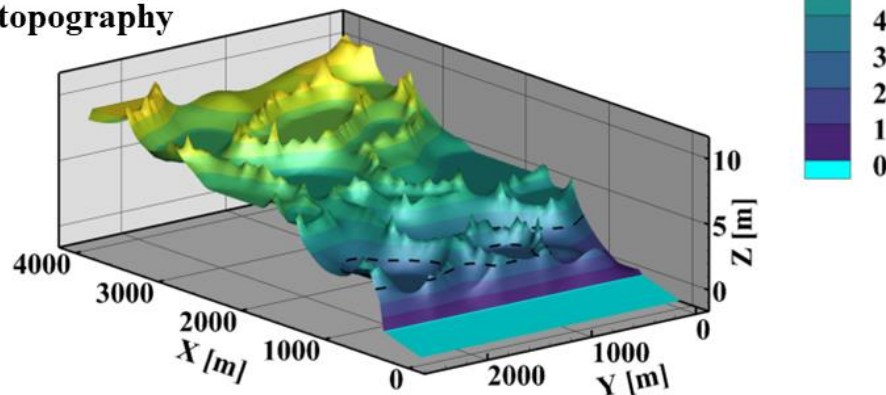
The sensitivity of the results to the topography and hydrogeologic parameters was tested, including freshwater influx ($0.01 < q_0 < 0.04$ m/d, Figure 3-2 and Table 1) and hydraulic conductivity- ($10 < K_x < 100$ m/d, Table 1, typical values for sandy beaches (Freeze & Cherry, 1979)). For the baseline hydraulic conductivity ($K_x=50$ m/d) the range of overall (land-to-sea) hydraulic gradients, calculated as q_0/K_x , was 0.0002 and 0.0008, on the lower side of typical coastal settings (roughly around 0.0010), and so the calculated hydraulic gradients in the current analysis are considered a conservative estimate. Two topographies (Figure 43) (Yu et al., 2016) were generated with ARCMAP 10.0 Geographic Information System (GIS) software (ESRI, 2011), using multigaussian random fields that were transformed (Zinn & Harvey, 2003) to connect either topographic highs or lows rather than the median topographic values as in the non-transformed multigaussian fields. The first topography, named “River” (Figure 4a3a), is characterized by surface depressions that connect to the sea. The topographic lows are connected, forming “river”-like patterns in the surface morphology), superimposed on the background slope of 0.0014. The second topography, “Crater” (Figure 4b3b), features connected crests surrounding disconnected surface depressions, such that the highs are connected, forming “crater” like shapes. The two topographies do not mirror each other (Figure 43), but represent reverse alongshore trends near the shoreline ($450 < X < 500$ m) in which the area around $0 < Y < 300$ m ($2200 < Y < 2500$ m) is the highest (lowest) for the River topography and lowest (highest) for the Crater topography. Comparisons with real topographies of the Delaware coastal plains (Yu et al. 2016) suggested that the River topography best represents real-world meso-topography. However, the Crater topography provides important insights to how meso-topography controls the evolution of head gradients during storm surges even though they are not necessarily representative of real systems. It is noted that exploring 4 values of hydraulic conductivity and two types of synthetic topographies may be a limited representation of natural systems.

300 For example, Xu et al. (2016) showed that topographic connectivity is a dominant factor in the vulnerability of coastal aquifers
 301 to storm surge salinization, and we consider here only two of the topographies simulated there. However, the tested
 302 topographies and conductivities in this work serve as a preliminary exploration of hypothetical conditions that are likely
 303 representative of many natural systems, but is certainly not inclusive. In extreme flooding events (e.g., tsunami), large-scale
 304 changes in surface morphology (e.g., landslides) may alter the pore-pressure distribution. These effects were excluded from
 305 the current work, as the simulated surface was considered constant throughout the simulation. Additionally, soil deformation
 306 and the resultant stress re-distribution were not considered in this model, as the hydrologic model (HGS) assumes constant
 307 porosity.

a. River topography



b. Crater topography



308
 309 **Figure 43:** (a) River and (b) Crater topographies as a function of the vertical Z , cross-shore X , and alongshore Y coordinates. Light
 310 blue is the offshore bathymetry, and the coastline is at $X=450$ m. The overall slope accounting for macro-topography is the same for
 311 both topographies, the average elevation at $X=4000$ m is ~ 5 m, making it a slope of $5/3550 \approx 0.0014$. The dashed black curve marks
 312 the $Z=3$ m contour, which is equal to the maximum surge-induced sea level (h_{max}).

315 For each simulation, the vertical hydraulic gradients (i_z in Equation 8) are calculated ~~for the modeled domain over a vertical~~
316 ~~slice along the coastline, i.e., the plane defined by $X=450$,~~ and normalized by the threshold defined by Equation 7 (i_c) to
317 calculate the SLF (Equation 8). As explained in Section 3 above, values of SLF that approach 1 are considered critical for
318 ~~liquefactionquicksand~~. When $SLF \ll 1$ the simulated surface theoretically is stable. Only upward, destabilizing velocities
319 (exfiltration) are considered, and so negative velocities were assigned a value of $i_z=0$.

320

321 **5.4 Results**

322 The baseline case ('River' topography with $q_0=0.02$ m/d ; $K_z=5$ m/d) includes a 3 m surge and simulates the resultant
323 changes in head gradients (Figure 54). During the ~~inundation-flooding~~ stage when sea level is increasing, the head gradients
324 increase landward in front of the moving surge, and in the flooded zone there is infiltration (head decreases downward, $\nabla h > 0$).
325 After the peak of the inundation, when the high-water levels begin to recede, downward gradients (i.e., head increases
326 downward, potentially destabilizing) develop underneath the still-water shoreline ($X=450$ m). These downward gradients
327 increase in magnitude as the water level recedes, and the subsurface system relaxes back to background levels (not shown in
328 Figure 54) within ~50 days for the high-K aquifers to ~500 days for the low-K aquifers, similar to prior simulations of storm
329 impacts (Robinson et al. 2014). The peak alongshore variation of the vertical hydraulic gradients occurs at the end of the
330 ~~inundation-flooding~~ ($t=8.4$ hr, Figure 54d). The vertical hydraulic gradients onshore of the ~~inundation-flooding~~ front during
331 run-up (Figure 5b4b) develop in subaerial areas~~-. As explained in section 3.1 above, and therefore~~ the calculated SLF for these
332 zones ~~is-should be~~ based on the saturated unit weight ($\gamma_{sat}=\gamma_{sub}+\gamma_{fw}$) of sediments rather than the submerged unit weight
333 (γ_{sub} , Equation 3), and the model-predicted ~~liquefaction-quicksand~~ may not occur in real systems because saturated soils are
334 more stable than submerged ones (Briaud, 2013).

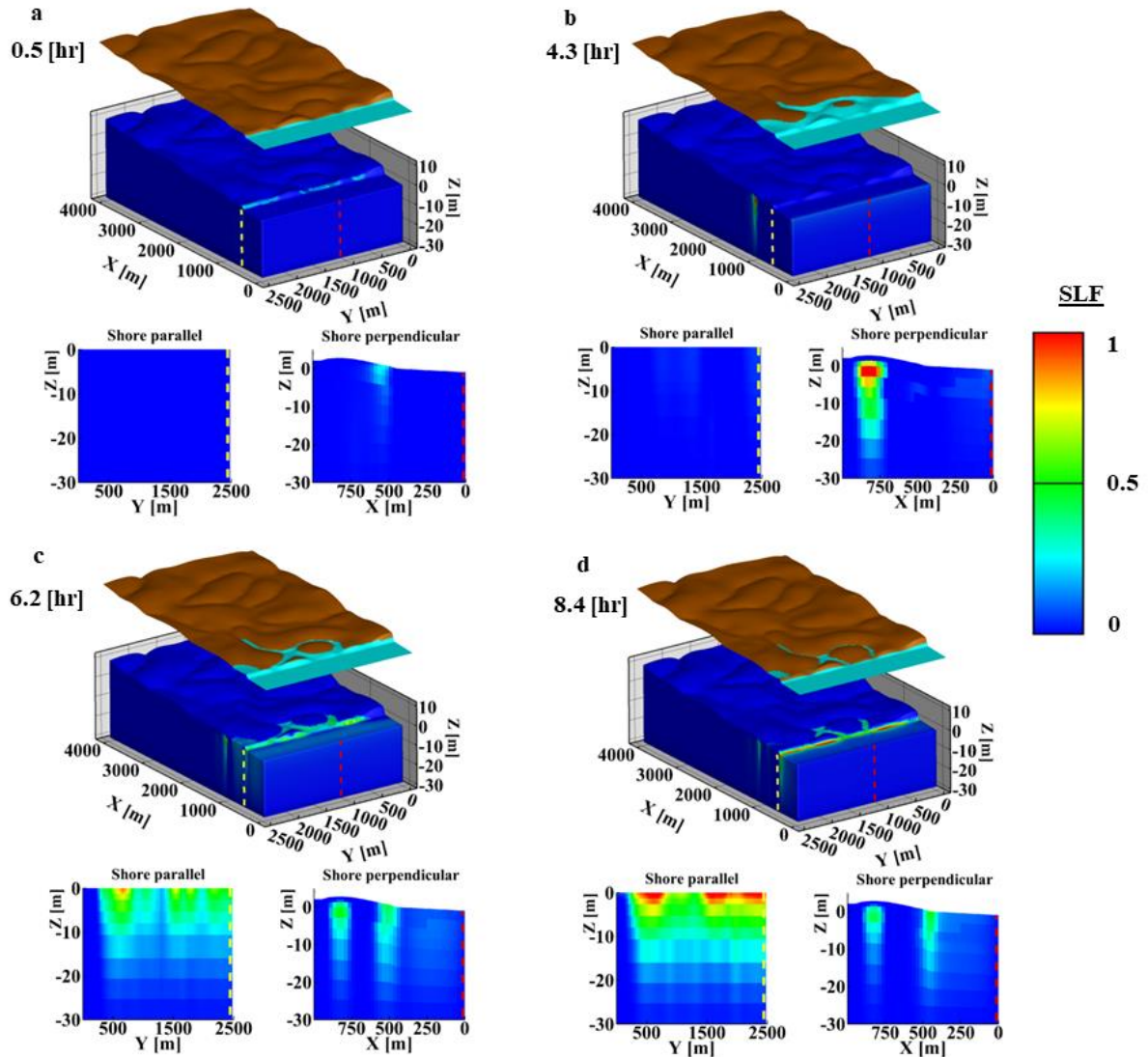


Figure 54: Surface [inundation-flooding](#) and vertical hydraulic gradients at (a) 0.5, (b) 4.3, (c) 6.2, and (d) 8.4 hr after the simulated surge begins (for the surge height at these times refer to Figure 32). In each panel, the surface domain is shown on top, the subsurface 3D domain and vertical gradients are shown below, and two cross sections through the subsurface are shown: shore-parallel (left in each panel) and shore-perpendicular (right). The locations of the sections are shown on the 3D plot as red dashed lines (for shore perpendicular) and yellow dashed lines (for shore parallel). The upper two panels are during the run-up stage and the lower are during the retreat stage. Refer to Figure 3-2 for the surge height at each time shown here. Note that downward gradients (head increases downward) are plotted as positive [values of SLF](#) and upward gradients (head increases upward) are plotted as zero [SLF](#).

The head changes (Δh in Figure 65) between the steady state and the peak of the [inundation-flooding](#) inversely follow the topography (black contours in Figure 6a-5a and b). For the highest topographic elements ($Y=0$ m for the “River” and $Y=2500$

346 m for the “Crater”), which are not inundated, the simulated heads are approximately equal to the maximum ocean level at the
 347 dune crest ($X \sim 460$ m), and decay inland over ~ 100 m, ~~roughly consistent with field observations (Figure 1).~~ The maximum
 348 head changes (purple colors in Figure ~~6a5a~~) inland of the shoreline ($X > 475$ m) at peak surge occur in the inundated topographic
 349 lows. Toward the end of the simulated surge ($t = 7.2$ hr, Figure ~~6b5b~~) the surge-induced ~~overpressures-increased pressures~~ are
 350 released in the topographic lows (low values of Δh in Figures ~~6b5b~~). The ~~temporal differences in head differences-between~~
 351 ~~surge and calm conditions~~ also are low in the topographic highs because the heads there did not rise significantly during
 352 ~~inundationflooding~~. In contrast, the intermediate topographic features show high head differences (dark purple in Figure ~~6b5b~~).
 353 The lowest near-shore ($450 \leq X \leq 500$ m, $900 \leq Y \leq 1200$ m) topography undergoes similar head changes during the peak surge for
 354 high and low K (compare Figure ~~6a1-5a1~~ with ~~6a35a3~~). However, in the low K case (Figure ~~6a35a3~~, ~~6b35b3~~), the heads are
 355 not released effectively as the surge recedes, and significant ~~excess-increased~~ heads of ~ 1 m difference remain near the end of
 356 the surge (compare Figure ~~6b3-5b3~~ with ~~6b1-5b1~~ for $X \sim 450$ m).
 357 When the surge has retreated ($t = 8.4$ hr), the head gradients at the dune toe (initial shoreline) ($X = 450$ m) reach their maximum
 358 (Figure ~~6e1-5c1~~-c3). In all simulations critical gradients ($SLF \rightarrow 1$, red zones in Figure ~~6-5~~ c1-c3) are simulated at some locations
 359 below the shoreline, supporting the findings of several recent field studies in which ~~momentary liquefaction-quicksand~~ was
 360 observed in response to inundation events (Sous et al., 2016; Yeh & Mason, 2014). The alongshore distribution of the surge-
 361 induced gradients is insensitive to the freshwater influx (q_0), even though the antecedent local hydraulic gradients differed
 362 by up to a factor of 4 between simulations (Figure A3 in the Appendices, note that the values of the antecedent local gradients
 363 are about an order of magnitude lower than the peak gradients). The depth and alongshore locations of the areas prone to
 364 ~~liquefaction-quicksand~~ (i.e., $SLF \sim 1$) are sensitive to the topography (compare Figures ~~6-5~~ a1,b1,c1 with a2, b2, and c2) and
 365 the hydraulic conductivity (compare Figures ~~6-5~~ a1,b1,c1 with a3, b3, and c3). The two topographies exhibit a similar spatial
 366 pattern of SLF (Figure ~~6e1-5c1~~ and c2) even though the differences in topography (Figure ~~43~~) cause significant differences in
 367 the surge-induced head changes (Figure ~~6-5~~ a1 and a2). For example, the area to the left of the domain ($Y \leq \sim 300$ m) is a
 368 topographic low in the Crater topography and undergoes significant head changes at the peak of the ~~inundation-flooding~~ (Figure
 369 ~~6a25a2~~), whereas for the River topography there is a topographic high for $Y \leq \sim 300$ m, which is not as strongly affected by the
 370 surge (Figure ~~6a15a1~~). However, in both cases this area is where the least significant vertical head gradients develop (Figure
 371 ~~6e1-5c1~~ and c2). ~~This means that a monotonic relationship cannot be assumed between topography and vulnerability (i.e., the~~
 372 ~~lowest/highest areas along the beach are not necessarily the most/least vulnerable).~~
 373 The hydraulic conductivity has a significant effect on the simulated surge-induced gradients (Figure A4 in the Appendices).
 374 Decreased hydraulic conductivity causes higher peak vertical gradients and changes the spatial (shore-parallel) distribution of
 375 the gradients (compare Figure ~~6e3-5c3~~ with ~~6e1-5c1~~, especially near $Y = 1000$ m, and also see Figure A4). Furthermore,
 376 decreasing hydraulic conductivity alters the depth Z_1 of “critical layers” with $SLF = 1$ (Equation 8) (compare Figure ~~6e3-5c3~~
 377 with ~~6e1-5c1~~). In the high-K simulations (Figure ~~6e1-5c1~~ and c2), the depth Z_1 of these “critical layers” with $SLF \sim 1$ ranges
 378 between 0 and 2.5 m, and in the low-K simulation (Figure ~~6e35c3~~) Z_1 is up to ~ 5 m.

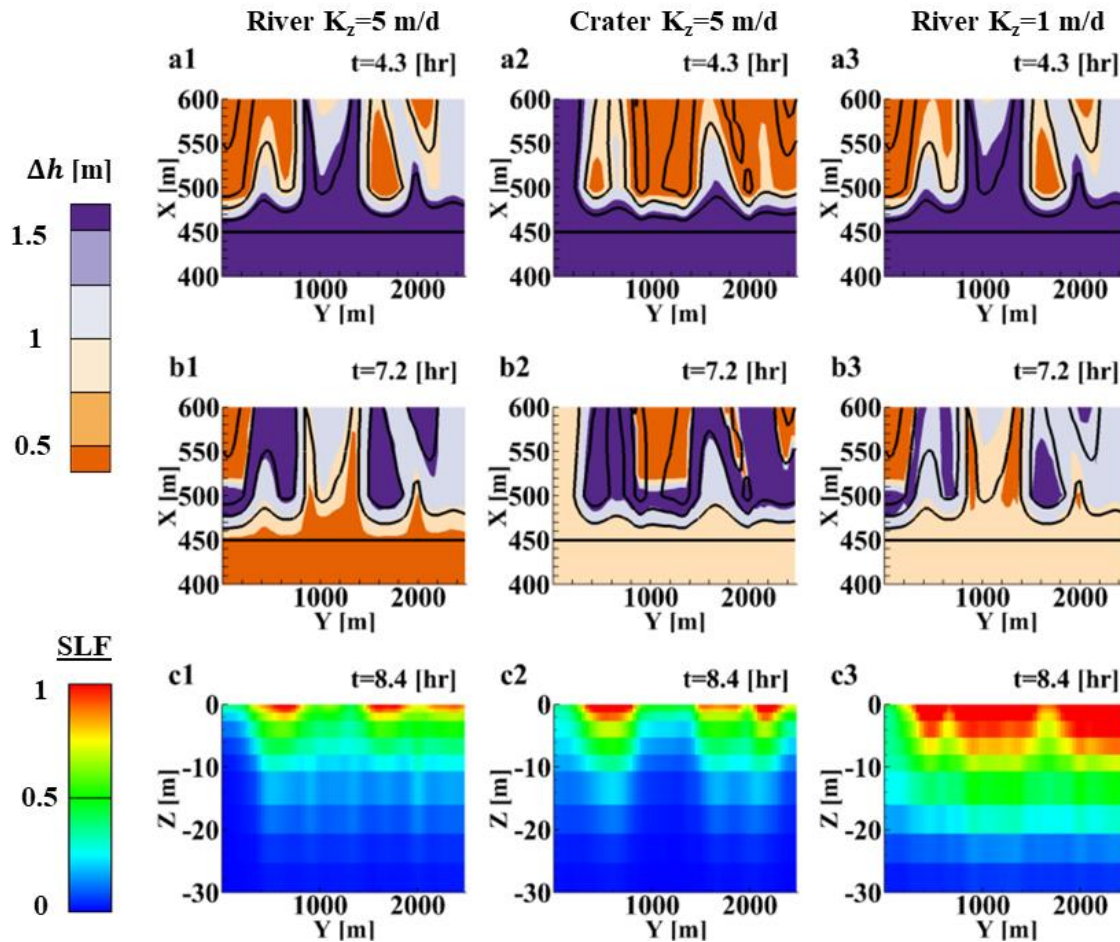
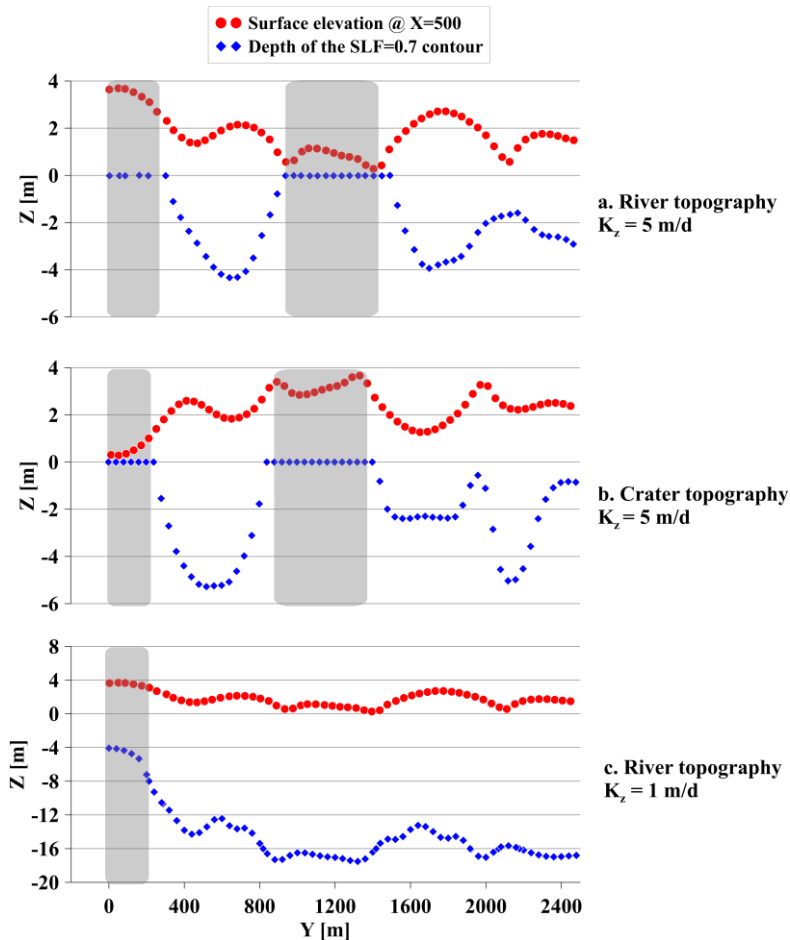


Figure 65: Top row (a1-a3): maps of the maximum near-surface head differences between those at the peak of the inundation flooding and the initial, pre-surge values (denoted Δh_1) as a function of the cross-shore X and alongshore Y coordinate. Middle (b1-b3): maps of the maximum subsurface head differences between those near the end of the surge ($t = 7.2$ hr, Figure 32) and the initial, pre-surge heads (denoted Δh_2) as a function of X and Y . Bottom (c1-c3): Liquefaction-quicksand potential SLF at the shoreline, $X = 450$ m, as a function of the vertical Z and alongshore Y coordinate. These 3 metrics are plotted for River topography with $K_z=5$ m/d (left, a1-a3), Crater topography with $K_z=5$ m/d (center, a2-c2) and River topography with $K_z=1$ m/d (right, a3-c3). In the upper and middle panels (map views a1-a3 and b1-b3) the black contours are surface elevation with 1 m intervals. The horizontal line at $X=450$ is the coastline ($Z=0$). The lower panels are plotted for $t=8.4$ hr, the time at which the vertical gradients peaked in all simulations all along the coastline.

The relationship between coastal topography and the surge-induced liquefaction-quicksand potential is evident when comparing the surface elevations 50 m landward of the coastline ($X=500$ m) and the peak vertical gradients below the coastline for different topographies and K 's (Figure 76). Here, the $SLF=0.7$ contour is used because for engineering applications it is required to design structures with a buffer to ensure a satisfactory factor of safety. Furthermore, using the $SLF=0.7$ provides

394 ~~better for~~ statistical stability ~~since~~ (there are more locations with $SLF \geq 0.7$ than with $SLF = 1$). For both topographies, when K
395 is high, SLF typically remains less than 0.7 (in Figure 7-6 where the blue diamonds = 0) at the shoreline adjacent to the highest
396 ($Z > 3$ m) and lowest ($Z < 1$ m) topographic elements (marked by gray rectangles in Figures 7a-6a and b), suggesting the
397 intermediate topographic features may lead to the strongest vertical hydraulic gradients and ~~liquefaction-quicksand~~ potential.
398 However, the height of intermediate features that produce high gradients may be dependent on the site and hydrogeological
399 parameters. For example, in the two simulations with higher K_z , 1-3 m topographic features are associated with most of the
400 significant surge-induced gradients (Figure 7a-6a and b). For the lower K_z case, significant gradients occur also below the
401 lowest area (Figure 7e6c), and only the highest area that is not inundated does not develop significant gradients (gray rectangle
402 in Figure 7e6c).



403
404 **Figure 7e6:** Topographic elevation at X=500 m (50 m onshore of the shoreline, red circles) and depth of the SLF=0.7 contour below
405 the shoreline (blue diamonds) versus alongshore coordinate Y for (a) the River topography with $K_z=5$ m/d, (b) Crater topography
406 with $K_z=5$ m/d, and (c) River topography with $K_z=1$ m/d. Deeper locations of the SLF=0.7 contour (blue diamonds) mean thicker
407 “critical layers”. The places where no significant critical layer develops (i.e., the elevation of the SLF=0.7 contour is $Z=0$) are marked
408 by gray rectangles.

6.5 Discussion

6.5.1 Alongshore variability

The simulations suggest that alongshore variability of the magnitudes of the vertical gradients is strongly associated with the coastal topography (Figures 5-74-6). To induce high gradients and deep critical layers when surge-induced increased pressures-heads are released, it is necessary to have inundation-flooding resulting in high infiltration and increased heads. Thus, topographic highs that are not inundated cannot develop high gradients (Figures 6-5 and 7-6). Meanwhile, overpressures-increased pressures often are released efficiently from inundated areas as the surge recedes. Topographic elements that are low enough to be inundated, but are also high enough to limit the post-surge exfiltration may prevent release of pressures with thicker porous medium that impedes flow, possibly explaining the correlation-of-liquefaction-link between quicksand potential with-and intermediate topographic features (1-3 m high for a 3 m surge). Topographic elements that are low enough to be inundated, but are also high enough to limit the post-surge exfiltration may prevent release of pressures, possibly explaining the correlation of liquefaction-quicksand potential with intermediate topographic features (1-3 m high for a 3 m surge). This explanation would suggest that the characteristic elevation of “intermediate features” would scale with the surge magnitude. Pressure releases also can be limited by low hydraulic conductivity. Thus, the simulations suggest the areas most susceptible to destabilization (i.e., deep critical layers) are those where topography is low enough to be inundated widely, and high enough that the pressure release is limited. An important factor that likely plays a role in this relationship between intermediate topography and critical gradients is the horizontal gradient. In places where horizontal hydraulic gradients can develop, a more efficient dissipation of surge-induced pressures may be expected, and therefore critical gradients are less likely. This may explain the absence of critical hydraulic gradients from steepest areas in the model, since these areas develop horizontal gradients. Horizontal gradients are important also when considering other modes of surface instability, such as shear failure. To assess the potential for shear failure, a Coulomb criterion must be derived, which is beyond the scope of the current study. Another factor that is known to control the vulnerability to storm-induced instability is the antecedent groundwater level which controls the infiltration capacity of flood waters (Cardenas et al., 2015). This may explain the absence of critical hydraulic gradients from the flatter areas of the model, leaving an intermediate range of topographies that are susceptible to surge-induced critical gradients. The range of susceptible topographic elements depends on hydraulic conductivity, which also has a sweet spot of vulnerability: A simulation with even lower hydraulic conductivity ($K_z=0.05$) showed that very low values of K limit the surge-induced infiltration and thus critical gradients develop only to a limited vertical extent and the alongshore variability (i.e., the dependency on onshore topography) diminishes (Figure A5 in the Appendices). This result has important implications to systems with higher clay content, since lower K values may mean that beach topography controls the overall vulnerability less than in sandy beaches.

65.2 Cross-shore spatiotemporal variability

During the flooding stage, negative vertical gradients (infiltration) that do not promote sediment instability occur at and seaward of the moving ~~inundation-flooding~~ front. Positive vertical gradients occur landward of the front (top right panel in Figure 54) owing to alteration of the pre-existing steady-state flow field (Figure 21) by the advancing ~~overpressures-increased pressures~~ from the surge. However, the simulated values of $SLF=1$ inland of the inundation front ~~are-do~~ not necessarily ~~imply sufficient to liquefy that quicksand is expected there in real systems~~~~the surface~~, because the actual weight of the unsubmerged soil is greater than ~~the uniformly-modeled~~ γ_{sub} (Equation 2). Nevertheless, the ~~liquefaction-quick sand~~ potential calculated here may still represent an underestimate, as Mory et al. (2007) showed that as little as 6% air content in the pores may reduce the ~~pressure head~~ required ~~pressure difference to~~ liquefy the sediment by 0.01 m. ~~While this 1 cm difference is an order of magnitude lower than the head changes discussed here (Figure 5), it is possible that in other hydrogeological settings the air content is more influential and therefore assuming fully saturated conditions may be a substantial underestimate of the quicksand potential.~~ This highlights the need to consider air contents in future studies. Furthermore, these inland processes, and the potential for liquefaction in these areas, may be affected by vegetation, trapping of gases, hysteresis of wetting and drying, and other processes that have not been considered here. Nevertheless, the presented approach demonstrates the feasibility and a pathway to implement the concept of surge-induced ~~quicksand momentary liquefaction~~ in a hydrological model that can predict variable-density groundwater flow in coastal and estuarine environments.

The receding water levels after the peak of the surge allow fast release of the elevated heads that developed in the inundated area, because the overlying burden of surge waters is removed abruptly. For all simulations at all alongshore locations, the positive head gradients simultaneously reached a maximum when the water had receded completely ($t=8.4$ hr, Figure 4d) and all the inundation water overburden was released. The rate of head release determines the hydraulic gradients that occur in the soil material, so that faster release of the ~~overpressures-increased pressures~~ allows less dissipation of elevated heads in the soil and therefore produces ~~lower positive head gradients~~~~thicker critical layers~~. As the water recedes, the highest release rates, and thus ~~increased over~~pressures, develop under the beach area, where the slope changes from a terrestrial average slope of 0.0014 to the seafloor slope of ~ 0.0022 (Figure 32). Thus, the simulations suggest the highest surge-induced gradients might be expected under convex topography, for example near the berm or near a scarp in the beach face.

65.3 Implications for coastal engineering

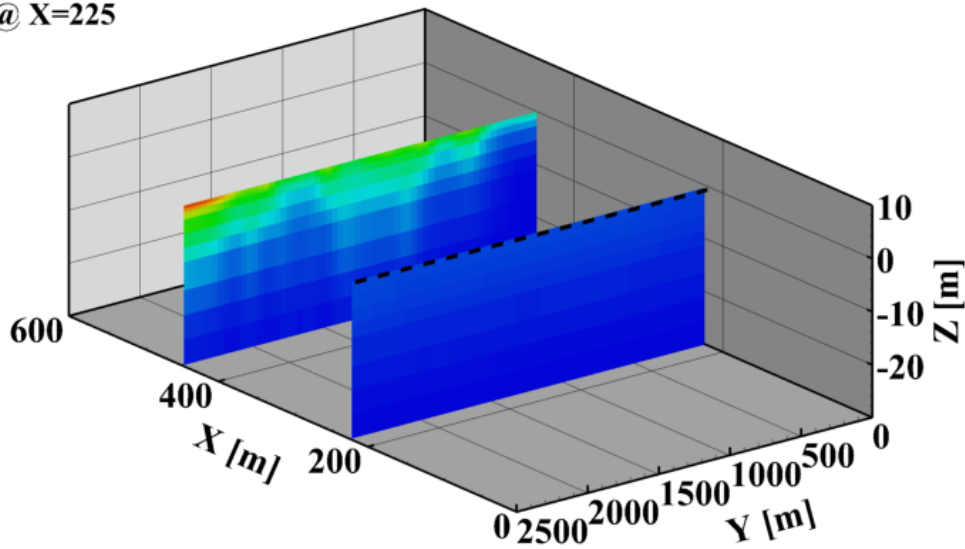
Most previous studies of extreme wave-induced pressurization in coastal environments focus on cross-shore variability (Sous et al., 2013, 2016; Turner et al., 2016; Yeh & Mason, 2014). Here, it is shown that under realistic hydrogeological conditions (surge height, topography, groundwater flow regime – all based on values that are commonly observed in natural systems) with alongshore varying topography there can be significant differences in storm-induced maximum vertical hydraulic gradients and in the depths of corresponding critical layers over small distances along the coastline (<500 m) (Figure 65). The simulations suggest that beach and dune morphology are important factors determining the spatial variability of high gradients.

472 Although low-lying coastal areas may endure the greatest flooding, the largest hydraulic gradients and the deepest ~~liquefaction~~
473 ~~quicksand~~ layers may occur at the toes of the intermediate-scale (1-3 m high for a 3 m surge) topographic features. ~~While our~~
474 ~~hydrologic model is generalized, a recent study has showed that numerical hydrologic modelling can be used to predict~~
475 ~~geomechanical risks induced by storm surges in specific settings too (Yang and Tsai, 2020).~~ While discussing practical
476 implications of the present analysis, it is important to remember that, as noted above, the model adopted here is a hydrological
477 model that does not explicitly simulate the soil dynamics and the surface and subsurface domains were assumed constant with
478 time through the simulations. This assumption overlooks other dynamic controls on the development of stresses, such as soil
479 deformation and surface erosion. Moreover, the analysis presented here isolates the vertical seepage component to calculate
480 the potential for ~~momentary soil liquefactionquicksand~~. In a 3D framework, horizontal seepage components likely come into
481 play and other failure mechanisms, such as shear failure, are likely too (Zen et al., 1998). However, for the conclusions drawn
482 here regarding the spatio-temporal distributions of surge-induced gradients, the hydrologic modeling provides an important
483 tool to study the hydrogeological aspect of the problem. The model could be further expanded to include other components in
484 future work.

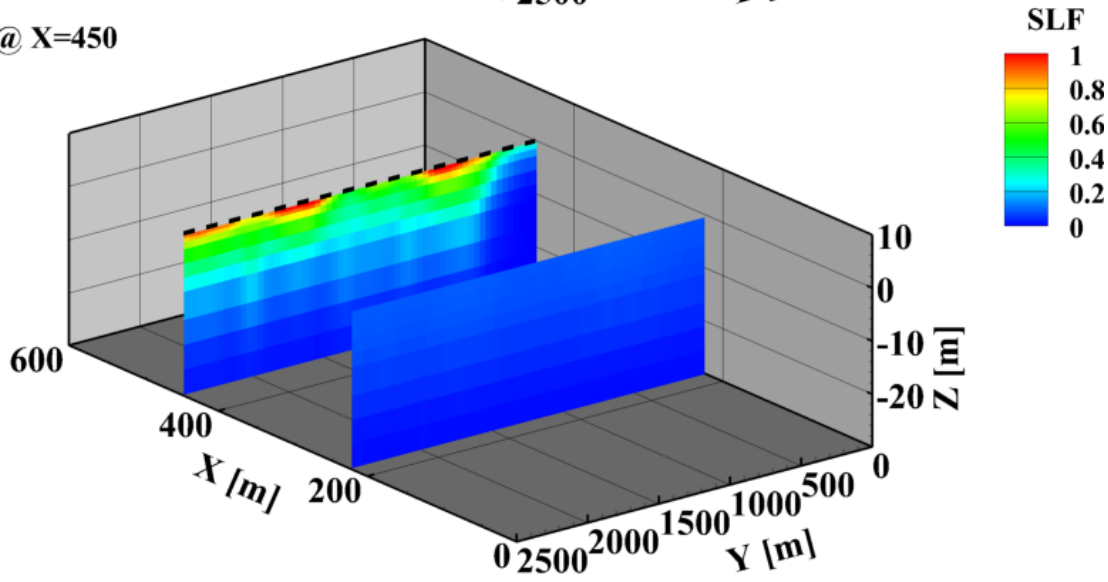
485 **7.6. Conclusions**

486 ~~Field measurements from Duck, North Carolina, show that during Hurricane Joaquin the groundwater flow regime at the ocean~~
487 ~~side was impacted substantially, and the hydraulic head gradient reversed its direction, followed by a period of recovery during~~
488 ~~which downward gradients (upward fluxes) were regenerated. This suggests that hydraulic gradients generated by s~~
489 ~~Storm~~ surges may substantially affect the ~~groundwater regime in flooded areas, which can reduce the~~ stability of beach surfaces. We
490 explored this idea and its generality by harnessing a robust hydrological model to simulate a generalized coastal system and
491 found that in the nearshore area, surge-induced hydraulic gradients may peak to critical levels that could potentially induce
492 ~~sand liquefactionquicksand~~. The locations where these critical, surge-induced gradients occur are transient, and depend on the
493 beach morphology and hydraulic conductivity. Both the elevation of topographic features and their permeability are important
494 factors in promoting ~~liquefactionquicksand~~. Elevations must be low enough to become inundated, and high enough to retain
495 elevated heads needed to build critical gradients. Similarly, hydraulic conductivity must be high enough to allow floodwater
496 to infiltrate, but low enough that water is not drained immediately such that critical gradients can persist. This alongshore
497 variability has not been observed in field measurements because the common approach in field studies is to measure the cross-
498 shore variability of hydraulic heads during storms. Importantly, this work presents a novel approach to bridge the gap between
499 coastal hydrology and coastal engineering, incorporating robust hydrogeological modeling in a geotechnical framework.

a. Coastline @ X=225

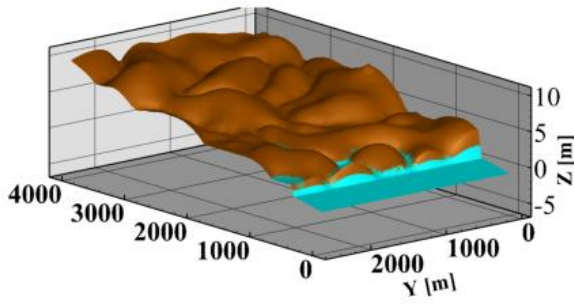


b. Coastline @ X=450

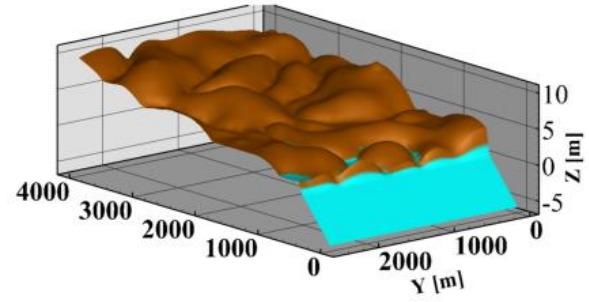


501
502 **Figure A1: Contours (color scale on the right) of peak SLF ($t=8.4$ hr) as a function of the vertical Z, cross-shore X, and**
503 **alongshore Y coordinate for (a) a simulation with the coastline at -0.5 m ($X = 225$ m) and (b) a simulation with the**
504 **coastline at 0 m ($X = 450$ m). The dashed black lines mark the coastline in each respective simulation. The slice with**
505 **high SLF values in (a) is not underneath the simulated coastline.**

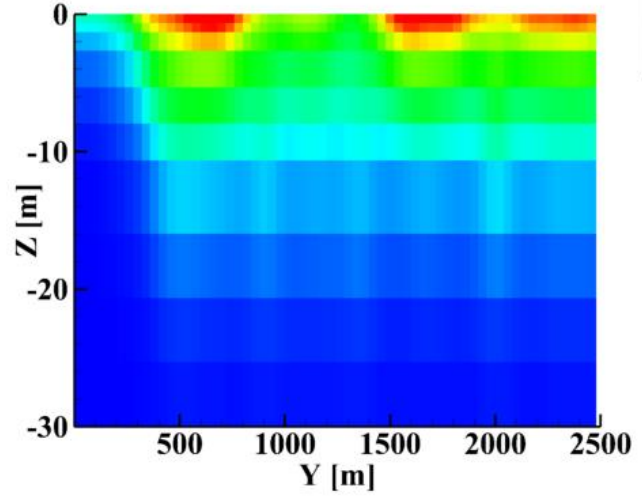
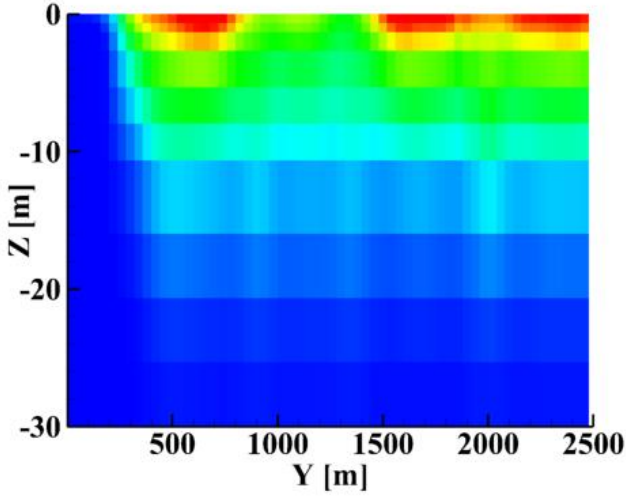
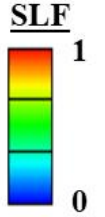
506



a. Bathymetric slope = 1/450



b. Bathymetric slope = 6/450



507

508 **Figure A2: Contours (color scale on the right) of peak SLF ($t = 8.4 \text{ hr}$) for a simulation with (a) bathymetric slope of**
 509 **$\frac{1}{450} \approx 0.002$ and (b) a simulation with a higher bathymetric slope ($\frac{6}{450} \approx 0.013$). The upper part of each panel shows**
 510 **the surface with the ~~inundation~~-flood water and the lower part is the vertical slice with the SLF values below the**
 511 **coastline ($X=450 \text{ m}$).**

512

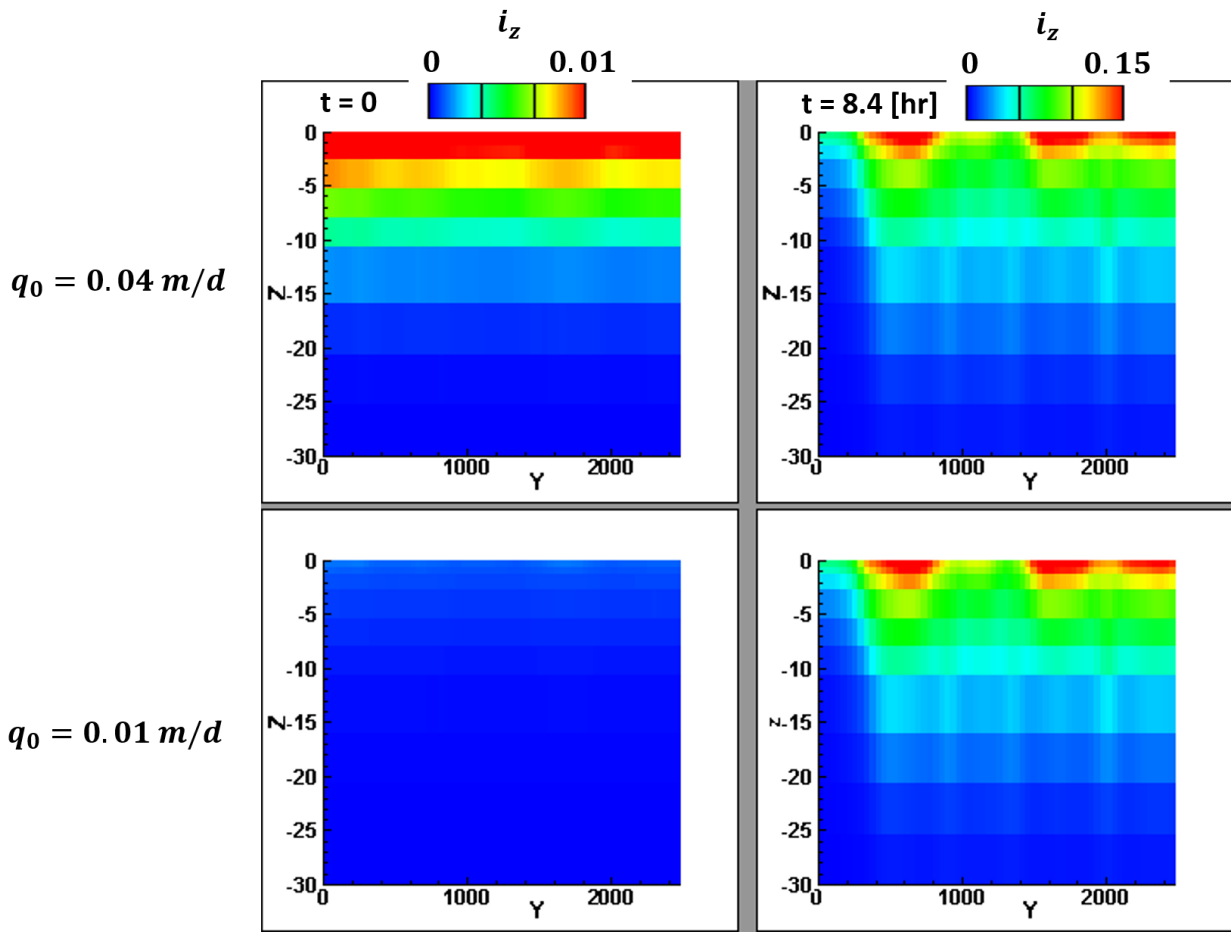
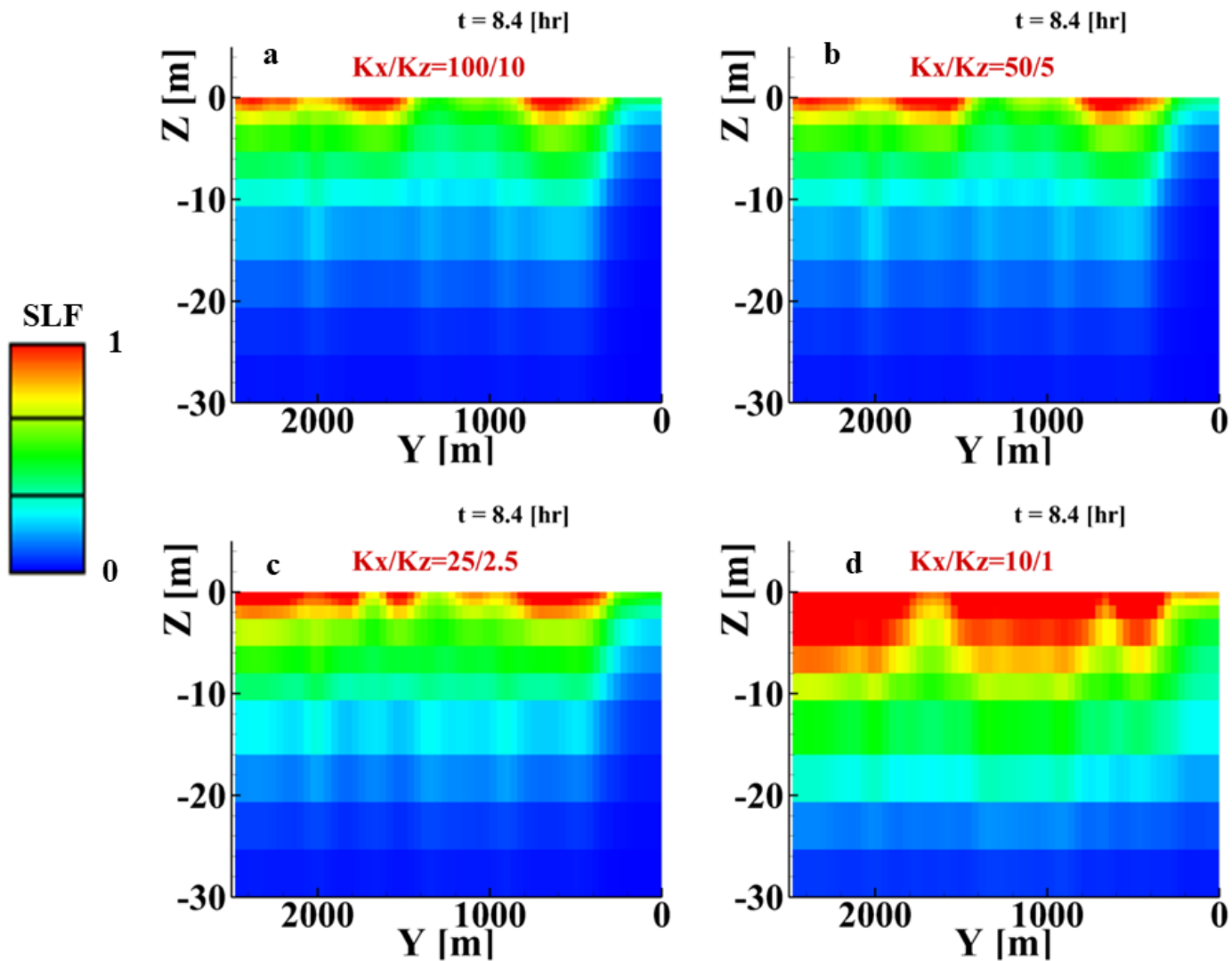


Figure A3: Contours (color scales on the top) of vertical hydraulic gradients (i_z) at $X = 450$ m (shoreline location) for the pre-surge conditions (left) and the end of the surge when gradients are maximum (right) as a function of vertical Z and alongshore Y coordinates. Note the different color scales between the pre-surge (left) and the peak (right) plots.



518
 519 **Figure A4: Contours (color scale on the left) of peak SLF (t=8.4 hr) vertical slices at the shoreline (X = 450 m) for Kx**
 520 **and Kz of (a) 100 and 10, (b) 50 and 5, (c) 25 and 2.5, and (d) 10 and 1 m/d.**
 521

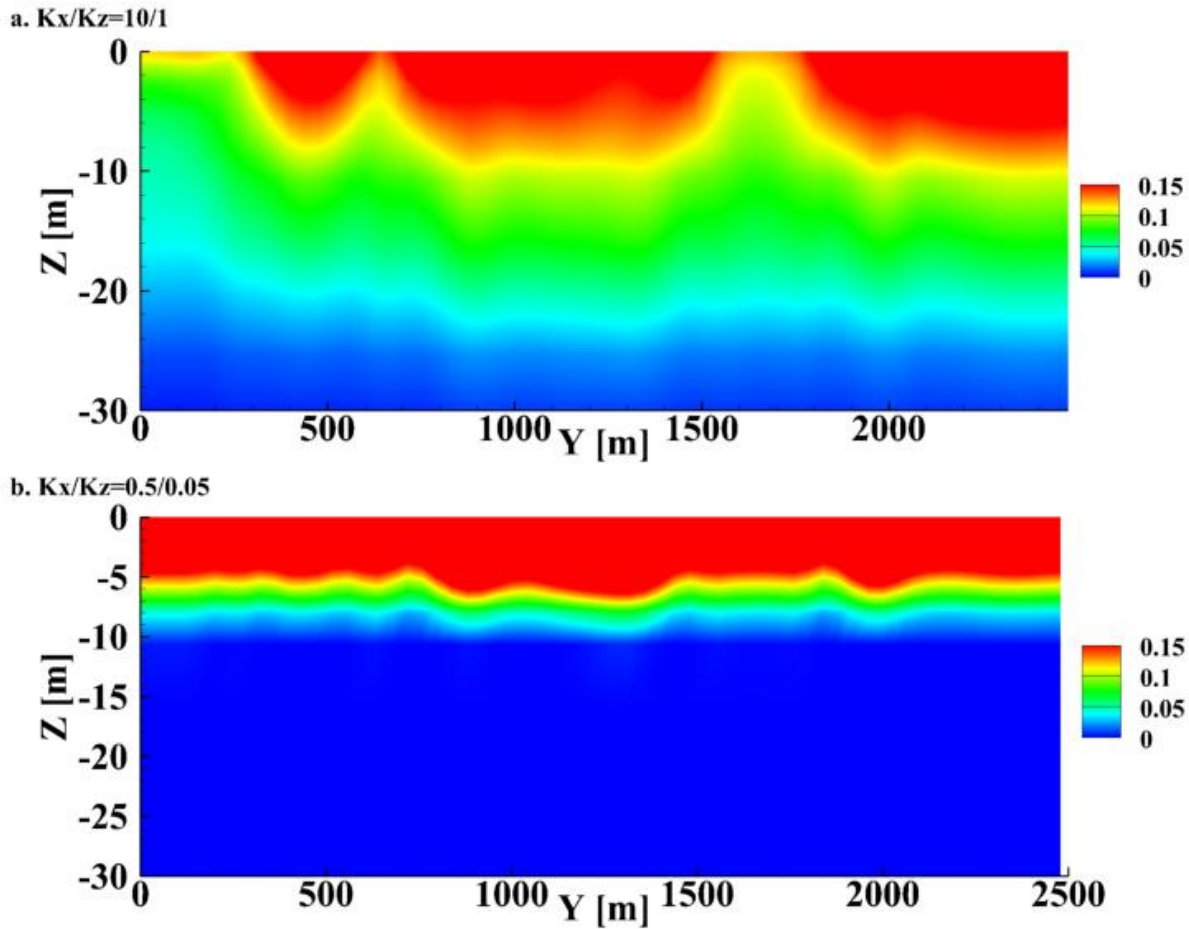


Figure A5: Contours (color scales on the right) of the maximum vertical hydraulic gradients (i_z) at $X = 450$ m (shoreline location) for (a) $K_z = 1$ and (b) $K_z = 0.05$) as a function of vertical Z and alongshore Y coordinates.

Author contribution

AP: conceptualization, investigation, visualization, formal analysis, writing (original draft); NS: conceptualization, formal analysis, writing (review and editing), funding acquisition; MF: formal analysis, writing (review and editing); BR: conceptualization, formal analysis, writing (review and editing), funding acquisition; SE: conceptualization, formal analysis, writing (review and editing), funding acquisition; RH; [Data curation](#), [vFormal analysis](#), [visualization](#), writing (review and editing); RF formal analysis, methodology; HM: conceptualization, formal analysis, writing (review and editing), supervision, funding acquisition, resources.

532 **Acknowledgments**

533 We thank the staff at the USACE Field Research Facility and the PVLAB field team for helping to deploy and maintain
534 groundwater wells. Funding was provided by The National Science Foundation (OCE1848650, OIA1757353, OCE1829136,
535 EAR1933010, CMMI-1751463, and a Graduate Research Fellowship), US Geological Survey (NIWR 2018DE01G), a
536 Vannevar Bush Faculty Fellowship, the US Coastal Research Program, and the Woods Hole Oceanographic Institution
537 Investment in Science Program.

538 **References**

539 Abdollahi, A., & Mason, H. B. (2020). Pore Water Pressure Response during Tsunami Loading. *Journal of Geotechnical and*
540 *Geoenvironmental Engineering*. [https://doi.org/10.1061/\(asce\)gt.1943-5606.0002205](https://doi.org/10.1061/(asce)gt.1943-5606.0002205)

541 Ataie-Ashtiani, B., Werner, A. D., Simmons, C. T., Morgan, L. K., & Lu, C. (2013). How important is the impact of land-
542 surface inundation on seawater intrusion caused by sea-level rise? *Hydrogeology Journal*. [https://doi.org/10.1007/s10040-013-](https://doi.org/10.1007/s10040-013-1021-0)
543 [1021-0](https://doi.org/10.1007/s10040-013-1021-0)

544 Bratton, J. F. (2010). The Three Scales of Submarine Groundwater Flow and Discharge across Passive Continental Margins.
545 *The Journal of Geology*, 118(5), 565–575. <https://doi.org/10.1086/655114>

546 Briaud, J.-L. (2013). *Geotechnical engineering: unsaturated and saturated soils*. John Wiley & Sons.

547 Burnett, W. C., Aggarwal, P. K., Aureli, A., Bokuniewicz, H., Cable, J. E., Charette, M. A., ... Turner, J. V. (2006).
548 Quantifying submarine groundwater discharge in the coastal zone via multiple methods. *Science of the Total Environment*,
549 367(2–3), 498–543. <https://doi.org/10.1016/j.scitotenv.2006.05.009>

550 Chini, N., & Stansby, P. K. K. (2012). Extreme values of coastal wave overtopping accounting for climate change and sea
551 level rise. *Coastal Engineering*, 65, 27–37. <https://doi.org/10.1016/J.COASTALENG.2012.02.009>

552 ESRI. (2011). *ArcGIS Desktop: Release 10*. Redlands, CA: Environmental Systems Research Institute. Redlands.

553 Freeze, R. A., & Cherry, J. A. (1979). *Groundwater*. Prentice-Hall.

554 Gelhar, L. W., Welty, C., & Rehfeldt, K. R. (1992). A Critical Review of Data on Field-Scale Dispersin in Aquifers. *Water*
555 *Resources Research*, 28(7), 1955–1974. <https://doi.org/10.1029/92WR00607>

556 Goren, L., Toussaint, R., Aharonov, E., Sparks, D. W., & Flekkøy, E. (2013). A general criterion for liquefaction in granular
557 layers with heterogeneous pore pressure. In *Poromechanics V - Proceedings of the 5th Biot Conference on Poromechanics*.
558 <https://doi.org/10.1061/9780784412992.049>

559 Guimond, J. A., & Michael, H. A. (2021). Effects of Marsh Migration on Flooding, Saltwater Intrusion, and Crop Yield in
560 Coastal Agricultural Land Subject to Storm Surge Inundation. *Water Resources Research*, 57(2).
561 <https://doi.org/10.1029/2020WR028326>

562 Housego, R., Raubenheimer, B., Elgar, S., Gorrell, L., Wadman, H., McNinch, J., & Brodie, K. (2018). *BARRIER ISLAND*
563 *GROUNDWATER*. *Coastal Engineering Proceedings*. <https://doi.org/10.9753/icce.v36.risk.10>

Iverson, R. M. (1995). can magma-injection and groundwater forces cause massive landslides on Hawaiian volcanoes, 66, 295–308.

Iverson, R. M., & Major, Jon J. (1986). Groundwater Seepage Vectors and the Potential for Hillslope Failure and Debris Flow Mobilization. *WATER RESOURCES RESEARCH*, 22(11), 1543–1548.

Iverson, R. M., & Reid, M. E. (1992). Gravity driven groundwater flow and slope failure potential: 1. Elastic Effective Stress Model. *Water Resources Research*, 28(3), 925–938. <https://doi.org/10.1029/91WR02694>

Mei, C. C., & Foda, M. A. (1981). Wave-induced responses in a fluid-filled poro-elastic solid with a free surface—a boundary layer theory. *Geophysical Journal of the Royal Astronomical Society*. <https://doi.org/10.1111/j.1365-246X.1981.tb04892.x>

Mory, M., Michallet, H., Bonjean, D., Piedra-Cueva, I., Barnoud, J. M., Foray, P., ... Breul, P. (2007). A field study of momentary liquefaction caused by waves around a coastal structure. *Journal of Waterway, Port, Coastal and Ocean Engineering*. [https://doi.org/10.1061/\(ASCE\)0733-950X\(2007\)133:1\(28\)](https://doi.org/10.1061/(ASCE)0733-950X(2007)133:1(28))

Orange, D. L., Anderson, R. S., & Breen, N. A. (1994). Regular Canyon Spacing in the Submarine Environment: The Link Between Hydrology and Geomorphology. *Geological Society of America Bulletin*, 4(2), 35–39.

Orange, D. L., Yun, J., Maher, N., Barry, J., & Greene, G. (2002). Tracking California seafloor seeps with bathymetry, backscatter and ROVs. *Continental Shelf Research*, 22(16), 2273–2290. [https://doi.org/10.1016/S0278-4343\(02\)00054-7](https://doi.org/10.1016/S0278-4343(02)00054-7)

Paldor, A., & Michael, H. A. (2021). Storm Surges Cause Simultaneous Salinization and Freshening of Coastal Aquifers, Exacerbated by Climate Change. *Water Resources Research*, 57(5), e2020WR029213. <https://doi.org/10.1029/2020WR029213>

Paldor, Anner, Aharonov, E., & Katz, O. (2020). Thermo-haline circulations in subsea confined aquifers produce saline, steady-state deep submarine groundwater discharge. *Journal of Hydrology*, 580. <https://doi.org/10.1016/j.jhydrol.2019.124276>

Rozhko, a. Y., Podladchikov, Y. Y., & Renard, F. (2007). Failure patterns caused by localized rise in pore-fluid overpressure and effective strength of rocks. *Geophysical Research Letters*, 34(22), L22304. <https://doi.org/10.1029/2007GL031696>

Sakai, T., Hatanaka, K., & Mase, H. (1992). Wave-induced effective stress in seabed and its momentary liquefaction. *Journal of Waterway, Port, Coastal and Ocean Engineering*, 118(2), 202–206. [https://doi.org/10.1061/\(ASCE\)0733-950X\(1992\)118:2\(202\)](https://doi.org/10.1061/(ASCE)0733-950X(1992)118:2(202))

Schorghofer, N., Jensen, B., Kudrolli, A., & Rothman, D. H. (2004). Spontaneous channelization in permeable ground: theory, experiment, and observation. *Journal of Fluid Mechanics*, 503(503), 357–374. <https://doi.org/10.1017/S0022112004007931>

Sous, D., Lambert, A., Rey, V., & Michallet, H. (2013). Swash-groundwater dynamics in a sandy beach laboratory experiment. *Coastal Engineering*. <https://doi.org/10.1016/j.coastaleng.2013.05.006>

Sous, D., Petitjean, L., Bouchette, F., Rey, V., Meulé, S., Sabatier, F., & Martins, K. (2016). Field evidence of swash groundwater circulation in the microtidal rousty beach, France. *Advances in Water Resources*. <https://doi.org/10.1016/j.advwatres.2016.09.009>

Stegmann, S., Sultan, N., Kopf, a., Apprioual, R., & Pelleau, P. (2011). Hydrogeology and its effect on slope stability along the coastal aquifer of Nice, France. *Marine Geology*, 280(1–4), 168–181. <https://doi.org/10.1016/j.margeo.2010.12.009>

598 Tebaldi, C., Strauss, B. H., & Zervas, C. E. (2012). Modelling sea level rise impacts on storm surges along US coasts.
 599 Environmental Research Letters. <https://doi.org/10.1088/1748-9326/7/1/014032>

600 Therrien, R., McLaren, R. G., Sudicky, E. A., & Panday, S. M. (2010). HydroGeoSphere. A three-dimensional numerical
 601 model describing fully-integrated subsurface and surface flow and solute transport. Groundwater Simulations Group.
 602 <https://doi.org/10.5123/S1679-49742014000300002>

603 Turner, I. L., Rau, G. C., Austin, M. J., & Andersen, M. S. (2016). Groundwater fluxes and flow paths within coastal barriers:
 604 Observations from a large-scale laboratory experiment (BARDEX II). Coastal Engineering.
 605 <https://doi.org/10.1016/j.coastaleng.2015.08.004>

606 Yang, J., Graf, T., Herold, M., & Ptak, T. (2013). Modelling the effects of tides and storm surges on coastal aquifers using a
 607 coupled surface-subsurface approach. Journal of Contaminant Hydrology, 149, 61–75.
 608 <https://doi.org/10.1016/j.jconhyd.2013.03.002>

609 Yang, J., Zhang, H., Yu, X., Graf, T., & Michael, H. A. (2018). Impact of hydrogeological factors on groundwater salinization
 610 due to ocean-surge inundation. Advances in Water Resources, 111, 423–434.
 611 <https://doi.org/10.1016/J.ADVWATRES.2017.11.017>

612 Yeh, H., & Mason, H. B. (2014). Sediment response to tsunami loading: Mechanisms and estimates. Geotechnique.
 613 <https://doi.org/10.1680/geot.13.P.033>

614 Yu, X., Yang, J., Graf, T., Koneshloo, M., O’Neal, M. A., & Michael, H. A. (2016). Impact of topography on groundwater
 615 salinization due to ocean surge inundation. Water Resources Research, 52(8), 5794–5812.
 616 <https://doi.org/10.1002/2016WR018814>

617 Zen, K., Jeng, D. S., Hsu, J. R. C., & Ohya, T. (1998). Wave-induced seabed instability: Difference between liquefaction
 618 and shear failure. Soils and Foundations, 38(2), 37–47. https://doi.org/10.3208/sandf.38.2_37

619 Zinn, B., & Harvey, C. F. (2003). When good statistical models of aquifer heterogeneity go bad: A comparison of flow,
 620 dispersion, and mass transfer in connected and multivariate Gaussian hydraulic conductivity fields. Water Resources Research.
 621 <https://doi.org/10.1029/2001WR001146>

622 Abdollahi, A., & Mason, H. B. (2020). Pore Water Pressure Response during Tsunami Loading. *Journal of Geotechnical and*
 623 *Geoenvironmental Engineering*. [https://doi.org/10.1061/\(asce\)gt.1943-5606.0002205](https://doi.org/10.1061/(asce)gt.1943-5606.0002205)

624 Briaud, J.-L. (2013). *Geotechnical engineering: unsaturated and saturated soils*. John Wiley & Sons.

625 Freeze, R. A., & Cherry, J. A. (1979). *Groundwater*. Prentice-Hall.

626 Gelhar, L. W., Welty, C., & Rehfeldt, K. R. (1992). A Critical Review of Data on Field-Scale Dispersion in Aquifers. *Water*
 627 *Resources Research*, 28(7), 1955–1974. <https://doi.org/10.1029/92WR00607>

628 Goren, L., Toussaint, R., Aharonov, E., Sparks, D. W., & Flekkøy, E. (2013). A general criterion for liquefaction in granular
 629 layers with heterogeneous pore pressure. In *Poromechanics V - Proceedings of the 5th Biot Conference on Poromechanics*.
 630 <https://doi.org/10.1061/9780784412992.049>

631 Guimond, J. A., & Michael, H. A. (2021). Effects of Marsh Migration on Flooding, Saltwater Intrusion, and Crop Yield in

632 Coastal Agricultural Land Subject to Storm Surge Inundation. *Water Resources Research*, 57(2).
633 <https://doi.org/10.1029/2020WR028326>

634 Paldor, A., & Michael, H. A. (2021). Storm Surges Cause Simultaneous Salinization and Freshening of Coastal Aquifers,
635 Exacerbated by Climate Change. *Water Resources Research*, 57(5), e2020WR029213.
636 <https://doi.org/10.1029/2020WR029213>

637 Yang, J., Graf, T., Herold, M., & Ptak, T. (2013). Modelling the effects of tides and storm surges on coastal aquifers using a
638 coupled surface-subsurface approach. *Journal of Contaminant Hydrology*, 149, 61–75.
639 <https://doi.org/10.1016/j.jconhyd.2013.03.002>

640 Yang, S., & Tsai, F. T. C. (2020). Understanding impacts of groundwater dynamics on flooding and levees in Greater New
641 Orleans. *Journal of Hydrology: Regional Studies*, 32. <https://doi.org/10.1016/j.ejrh.2020.100740>

642 Yu, X., Yang, J., Graf, T., Koneshloo, M., O’Neal, M. A., & Michael, H. A. (2016). Impact of topography on groundwater
643 salinization due to ocean surge inundation. *Water Resources Research*, 52(8), 5794–5812.
644 <https://doi.org/10.1002/2016WR018814>

645 Zen, K., Jeng, D. S., Hsu, J. R. C., & Ohya, T. (1998). Wave-induced seabed instability: Difference between liquefaction
646 and shear failure. *Soils and Foundations*, 38(2), 37–47. https://doi.org/10.3208/sandf.38.2_37

647